Ore Geology Reviews 92 (2018) 42–60

Contents lists available at ScienceDirect

Ore Geology Reviews

journal homepage: www.elsevier.com/locate/oregeorev

A stand-alone Co mineral deposit in northeastern Hunan Province, South China: Its timing, origin of ore fluids and metal Co, and geodynamic setting

Shaohao Zou[a,b,c], Fenghui Zou[a,b], Juntao Ning[d], Teng Deng[a,b], Deshui Yu[a,b], Tingwei Ye[a,b], Deru Xu[a,*], Zhilin Wang[e]

[a] CAS Key Laboratory of Mineralogy and Metallogeny, Guangzhou Institute of Geochemistry, Chinese Academy of Sciences, Guangzhou 510640, China
[b] University of Chinese Academy of Sciences, Beijing 100049, China
[c] Department of Earth and Environmental Sciences, University of Windsor, Windsor, Ontario N9B 3P4, Canada
[d] Team 402, Hunan Geology and Mineral Resources Exploration and Development Bureau, Changsha 410014, China
[e] Schools of Geosciences and Info-Physics, Central South University, Changsha 410083, China

ARTICLE INFO

Keywords:
Ore-fluid evolution
$^{40}Ar/^{39}Ar$ dating
Mineralogy
Hengdong cobalt deposit
South China

ABSTRACT

The Hengdong cobalt (Co) deposit, located in northeastern Hunan Province of South China, is hosted by the low-grade metamorphic volcaniclastic sedimentary rocks of the early Neoproterozoic Lengjiaxi Group. The Co orebodies strictly controlled by the NE- to ENE-trending Changsha-Pingjiang deep fault zone (CPDFZ) and its secondary structures. Occurring in altered breccias and cataclasites with similar mineral assemblages, Co mineralization is characterized by zoned alteration with predominant silicification and chloritization proximal to the orebodies, and sericitization and carbonatization distal from the mineralization. The integrated field and microscope observations reveal three hydrothermal stages marked by quartz + pyrite + muscovite ± chalcopyrite of the early-stage mineralization (E-stage), quartz + polymetallic sulfides + chlorite of the middle-stage mineralization (M − stage), and quartz + chlorite + carbonate of the late-stage mineralization (L-stage). Muscovite from both the E-stage Co-bearing altered breccia and the CPDFZ mylonite yield ^{40}Ar–^{39}Ar plateau ages of 124.7 ± 0.6 Ma (1σ) and 130.3 ± 1.4 Ma (1σ), respectively, indicating an early Cretaceous mineralization likely associated with the last movement of CPDFZ strike-slip shearing. The $\delta^{34}S$ values of pyrite and chalcopyrite ranging from −1.5 to −15.9% with a majority between −7.5 and −15.9%, and the lead isotope compositions of the pyrite ($^{206}Pb/^{204}Pb$ = 18.156–18.761, $^{207}Pb/^{204}Pb$ = 15.645–15.662 and $^{208}Pb/^{204}Pb$ = 38.469–39.172) overlapping with those of upper crust, indicate a main crust-derived source. The chemical compositions of pyrite further indicate the ore fluids and metal Co of the Hengdong deposit are most likely linked to the meta-mafic and volcanic rocks of the Neoarchean to Paleoproterozoic Lianyunshan Group, but with a contamination by the wall rocks of Lengjiaxi Group and Lianyunshan granitoids. Fluid inclusion investigations from Hengdong deposit reveal the decreasing homogenization temperatures from 250 to 320 °C (peak of 280–300 °C) at the E stage, through ~220–320 °C (peak of 270–300 °C) at the M stage, and to ~150–230 °C at the L stage without obviously salinity (7.0–15 wt% NaCl equiv.) changed. In the M − stage, the presence of coexisting LV inclusions and V-rich inclusions with the similar homogenization temperature, consistent with the chlorite geothermometry data, is interpreted to be the result of fluid immiscibility, which was caused by cyclic pressure release during fault-zone movement. Combined with the Late Mesozoic tectonism of South China, the present data support the Hengdong deposit formed under an extension-associated tectonic regime most likely induced by slab roll-back of the subducted Paleo-Pacific Plate during the early Cretaceous. This extensional event not only caused the reactivation of the pre-existing structures as manifested by the CPDFZ characteristic of stress transformation from compression to extension but also likely resulted in the release of large amounts of Co-bearing ore fluids from the Proterozoic or older volcanogenic rocks. When the ore fluids migrated along the CPDFZ and its secondary faults, the decompression (adiabatic cooling) of the hydrothermal fluids shifted the ore fluid to the immiscibility field, significantly reduced the degree of cobalt undersaturation, and caused cobalt to precipitate, which finally formed the Hengdong Co mineral deposit.

* Corresponding author.
E-mail address: xuderu@gig.ac.cn (D. Xu).

https://doi.org/10.1016/j.oregeorev.2017.11.008
Received 3 May 2017; Received in revised form 30 October 2017; Accepted 8 November 2017
Available online 10 November 2017

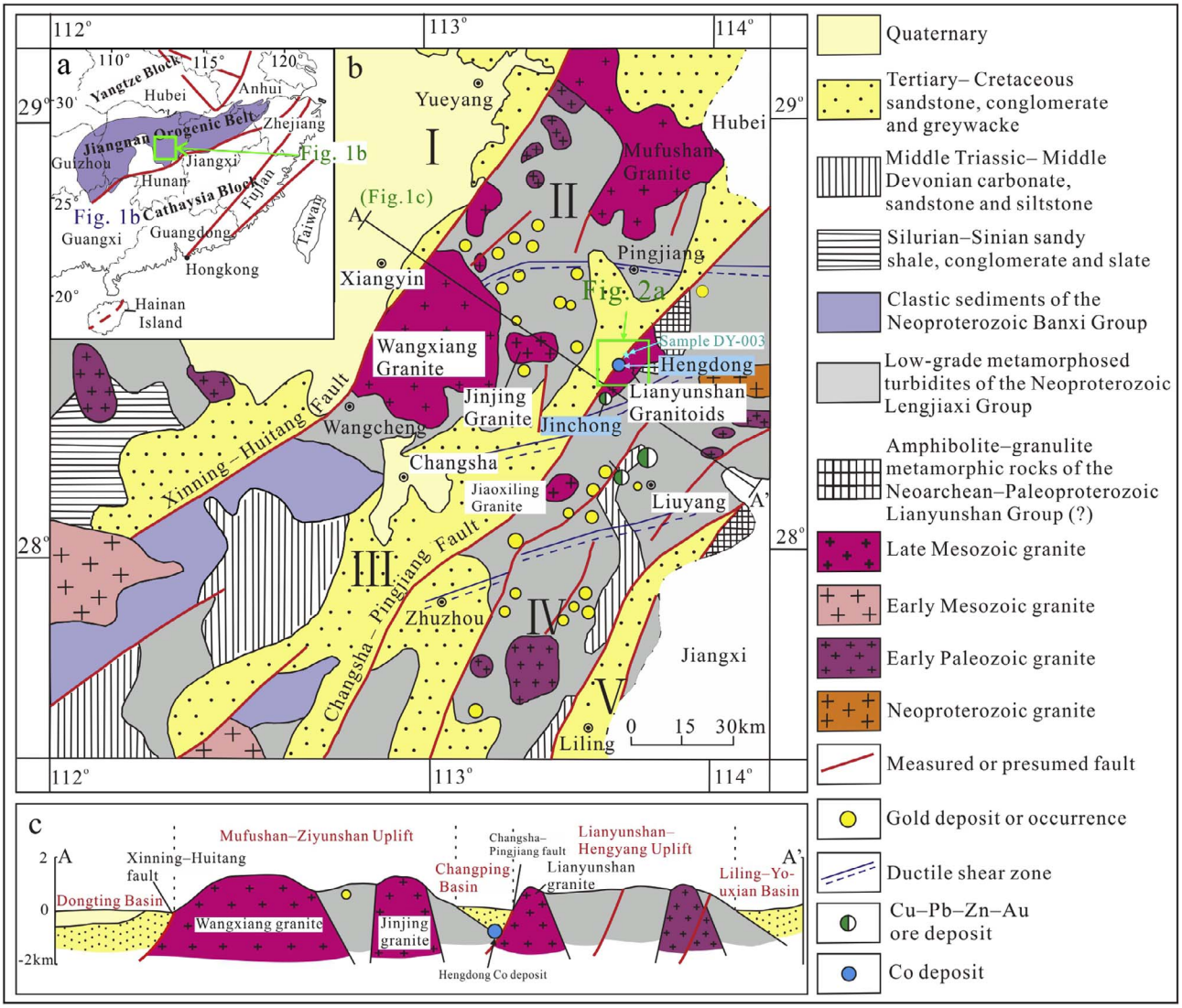

Fig. 1. (a) Sketch map of South China showing the tectonic relationship between the Yangtze and the Cathaysia Blocks, modified after Chen and Jahn (1998). The green area represents the Jiangnan orogenic belt (JOB) and the exposed Neoproterozoic volcaniclastic sediments in this area. (b) Enlarged map showing the structures, Proterozoic and magmatic rocks and ore deposits in the northeastern Hunan province, South China, modified after He et al. (2004) and Xu et al. (2009). (**I**) = Dongting Basin, (**II**) = Mufushan-Ziyunshan Uplift, (**III**) = Changping (Changsha-Pingjiang) Basin, (**IV**) = Lianyunshan-Hengyang Uplift and (**V**) = Liling-Youxian Basin; (c) Cross section of A-A' in Fig. 1b. (For interpretation of the references to colour in this figure legend, the reader is referred to the web version of this article.)

1. Introduction

Cobalt (Co), a critical and strategic metal, is one of the most important elements in aerospace and mechanical industry due to its property of high temperature resistant and corrosion resistant. As a compatible siderophile and chalcophile element, the main source of cobalt (Co) is hardly formed as stand-alone deposits, but as a by-product in four main ore-deposit types (Feng and Zhang, 2002; Wang et al., 2017 and references therein), i.e., sediment-hosted stratiform Cu–Co deposits, magmatic Cu–Ni–Co sulfide deposits (Naldrett et al., 2000), lateritic Ni–Co deposits (Dzemua and Gleeson, 2012; Al-Khirbash, 2015) and volcanic-hosted massive sulfide (VHMS) Cu–Ni–(Co) deposits (Marques et al., 2007). It is generally agreed that Co is derived from sulfides or mafic–ultramafic complexes (Naldrett, 1999; Dzemua and Gleeson, 2012) that are generally interpreted to be the source of Co. However, it is poorly documented as stand-alone Co mineral system.

The Jiangnan Orogenic Belt (JOB) of South China (Fig. 1a) has become one of the important polymetallic regions in South China (Xu et al., 2017 and references therein), because of its package of hydrothermal Au, Au–Sb and Au-Sb–W deposits mainly hosted by Neoproterozoic volcaniclastic and sedimentary rocks, porphyry- and skarn-type Cu–Au–Pb–Zn deposits and W–(Cu) deposits associated with Mesozoic granitoids, and Cu–Ni sulfide deposits related to mafic/ultramafic rocks. In the last two decades, numerous Au, Cu, Pb–Zn and Co deposits have also been discovered in northeastern Hunan Province of the central JOB (Fig. 1b). The discovery of the primary Co-related deposits, represented by the Hengdong Co and Jingchong Co–Cu deposits (Wang et al., 2017), has publicized that economically significant Co mineralization also occurs in the JOB (Ning, 2002). Subsequently, associated studies (Wang et al., 2017) were carried out on ore geology, ore-controlling structure and ore geochemistry, in order to evaluate ore-forming processes and genesis of these Co-related deposits. The Hengdong Co deposit, located in northeastern Hunan Province of the JOB, is sited within the NE- to ENE-trending Changsha-Pingjiang deep fault zone (CPDFZ) developed in the low-grade metamorphic volcaniclastic sedimentary rocks of the early Neoproterozoic Lengjiaxi Group (Fig. 1b). This deposit differs from the typically Co producing deposits, because (1) it contains proved metal Co reserves of more than 12,400 t with an average grade of 0.04 wt% Co (locally up to 4.10 wt% Co); (2)

however, Au and Cu are the by-product commodities, and (3) the Co orebodies are strictly controlled by fault zones or its secondary structures.

The fundamental geological and mineralizing characteristics of the Hengdong deposit were briefly described in Jin and Zhang (2000), Fu (2001), Ning (2002), Xu et al. (2009) and Yi et al. (2010), but these studies, which led to a controversy on ore genesis of the Co-related deposits, mostly came from the field investigations and rarely from ore geochemical data. Moreover, less attention has been paid to Co mineralization when compared with that to the gold mineralization in the northeastern Hunan Province, up to now (e.g., Deng et al., 2017; Xu et al., 2017 and references therein). Consequently, details about the mineralizing age, ore-forming fluids and metals, and metallogenetic processes of this deposit are not available so far. In this contribution, we first carried out ^{40}Ar–^{39}Ar dating on cobalt-related muscovite of hydrothermal origin to constrain the mineralization timing of the Hengdong deposit. Then an integrated analysis on mineral chemistry, sulfur (S) and lead (Pb) isotopes, and fluid inclusions were implemented, in an attempt to provide insights into the nature and origin of ore fluids as well as the source region(s) of the metal Co. Combined with regional geological and structural evidence, a genetic model associated with the late Mesozoic extensional event(s) is proposed to guide future mineral exploration.

2. Regional geological setting

South China Block (SCB; Fig. 1a) is composed of the Yangtze Block in the northwest and the Cathaysia Block in the southeast, which were amalgamated during the Neoproterozoic (Li et al., 2009). The JOB has been generally considered to represent the Neoproterozoic collisional belt between the Yangtze and the Cathaysia blocks, and its geological features and tectonic evolution have been described in detail by Zhao and Cawood (2012) and Zhao et al. (2016). Located in the central segment of the JOB (Fig. 1a and b), the northeastern Hunan Province, is mainly characterized by the Neoproterozoic successions dominated by volcaniclastic and sedimentary rocks with greenschist facies metamorphism. These Neoproterozoic successions comprise the early Neoproterozoic (ca. 850–825 Ma; Wang et al., 2007a, 2008, 2011a; Zhou et al., 2009; Gao et al., 2008, 2011; Zhang et al., 2012; Zhang and Zheng, 2013) Lengjiaxi Group and the middle Neoproterozoic (ca. 815 Ma; Wang et al., 2003, 2006b; Gao et al., 2011) Banxi Group. Structurally, the Lengjiaxi Group is characterized by high-angle tight linear belts and isoclinal overturned folds, which contrast with the upright and open folds developed in the unconformably overlying Banxi Group (Zhao and Cawood, 2012). This angular unconformity has been interpreted as the result of the amalgamation between the Yangtze and the Cathaysia blocks to form the united SCB (Zhao and Cawood, 2012; Zhao, 2015). Underlying the Lengjiaxi Group likely is an older crystalline basement, including the Paleoproterozoic Jianxichong Group and the Neoarchean to Paleoproterozoic Lianyunshan Group (Jia and Peng, 2005). The Jianxichong Group (ca. 2.0–1.8 Ga; Sm-Nd isochron and SHRIMP zircon U-Pb ages) occurs in the Wenjiashi area and consists of meta-tholeiitic basalts intercalated with meta-volcaniclastics and magnetite quartzites (Jia and Peng, 2005). The Neoarchean to Paleoproterozoic Lianyunshan Group, a suite of volcanic and sedimentary succession of amphibolite-facies metamorphism, is exposed in the Lianyunshan area of the northeastern Hunan Province, and in return intruded by the Late Mesozoic Lianyunshan granitoids (Fig. 1b; HNBGMR, 1988; Jia and Peng, 2005).

Multistage granites, intruding into the Lengjiaxi Group, are widespread in northeastern Hunan Province (Fig. 1b). The emplacement ages for these granites include the early to late Neoproterozoic represented by the Getengling pluton of ca. 845 Ma ages (our unpublished data), the Caledonian by the Banshanpu and Hongxiaqiao plutons of ca. 434–420 Ma ages (Guan et al., 2014; Li et al., 2015), and the Yanshanian by the Mufushan, Wangxiang, Jinjing and Lianyunshan plutons of ca. 154–137 Ma ages (Jia et al., 2003; Peng et al., 2004; Shi et al., 2013; Wang et al., 2014; Deng et al., 2017). The Yanshanian granitiods, the most abundant igneous rocks in the region, were intruded within the uplifts of the Basin-and-Range structures (Wang et al., 2017). Abundant mafic/ultramafic rocks and bimodal volcanic rocks of late Yanshanian ages (ca. 136–80 Ma) also occur in the northeastern Hunan Province (Jia et al., 2003; Wang et al., 2008). These Yanshanian granitoids and mafic rocks were considered to have formed in an extensional tectonic setting due to the rollback of the subducted Paleo-Pacific plate (Xu et al., 2009; Wang et al., 2014).

The northeastern Hunan Province is characterized by a NE- to ENE-trending echelon “Basin-and-Range” tectonic framework, which is composed of three basins and two uplifts, from NW towards SE as follows: Miluo graben basin (I), Mufu-Wangxiang uplift (II), Changsha-Pingjiang graben basin (III), Liuyang-Hendong uplift (IV) and Liling-Youxian graben basin (V; Fig. 1c). These basins and uplifts are delimited by a few NE- to ENE-trending crustal scale strike-slip shear fault zones such as the Xinning-Huitang and the Changsha-Pingjiang deep fault zone (Fig. 1c), the latter controlling the Hengdong and Jingchong deposits. This CPDFZ section separates the Lianyun-Hendong uplift from the Changsha-Pingjiang graben basin, and shows strong ductile-shear deformation and mylonitization (Xu et al., 2009). Structural and chronological analyses (Zhang, 1991; Fu et al., 1999; Xu et al., 2009) indicate that since the Mesozoic, the CPDFZ might be subjected to the late Triassic-Jurassic NNE-trending sinistral transpressional shearing and the Cretaceous NE-trending extensional shearing, most likely in response to the two important tectonic events, i.e., the Triassic collision between the South China and the North China blocks, and the subduction with subsequent slab roll-back of the paleo-Pacific plate beneath the Asian continental margin, respectively. This thus suggests that the CPDFZ underwent reactivation processes (Baudon and Cartwright, 2008) due to the multistage tectonic development of South China.

A number of Au-, Cu- and Co- (polymetallic) mineral systems have been discovered in northeastern Hunan Province (Fig. 1b), including the fault-controlled Wangu and Huangjindong gold deposits (Deng et al., 2017), the porphyry Cu-Pb-Zn deposits (Qibaoshan and Aoyushan), and the hydrothermal-related Co-(Cu)-(Au) deposits (Jingchong, Hengdong and Dayan) (Yi et al., 2010; Wang et al., 2017).

3. Deposit geology

The Hengdong deposit is situated at the CPDFZ, which consists of numerous parallel NE-trending faults (Figs. 1b and 2a), together with the occurrence of mylonites, cataclasites and silicified breccias. In the Hengdong district, the NE- to ENE-trending CPDFZ consists of a swarm of fractured zones, with the F_1, F_2, F_3 and F_4 faults acting as the main ore-controlling structures (Fig. 2a). The most economically significant fractured zone in association with Co mineralization is the F_2, which has a width of 10–100 m, tends to strikes N30°E and dips 40° NW. The F_2 fractured zone is characterized by well-developed altered cataclasite belt (C*b*) in the northwest and altered tectonic breccia belt (B*b*) in the southeast (Fig. 2b). The former is characterized by the fracture zones in which foliation, mylonitization, and tectonic lenses are developed, whereas the latter is featured by widespread hydrothermal alteration zones composed of silicified and/or chloritized breccias and chloritized quartzites. In the footwall of the F_2, i.e., the transition between the Lianyunshan pluton and the C*b*, a migmatization belt (M*b*) which generally consists of grey-green, dark-green banded migmatites and dark-grey migmatites has also been observed in some local areas (Fig. 2a).

To the southeast, the Hengdong district was *syn*-kinematically intruded by the Late Mesozoic Lianyunshan plutons (Fig. 1b), which are composed of biotite monzogranite, two mica monzogranite and granodiorite. The outcropping rocks in the study area include the Quaternary cover, the Cretaceous Hengyang Group and the Neoproterozoic

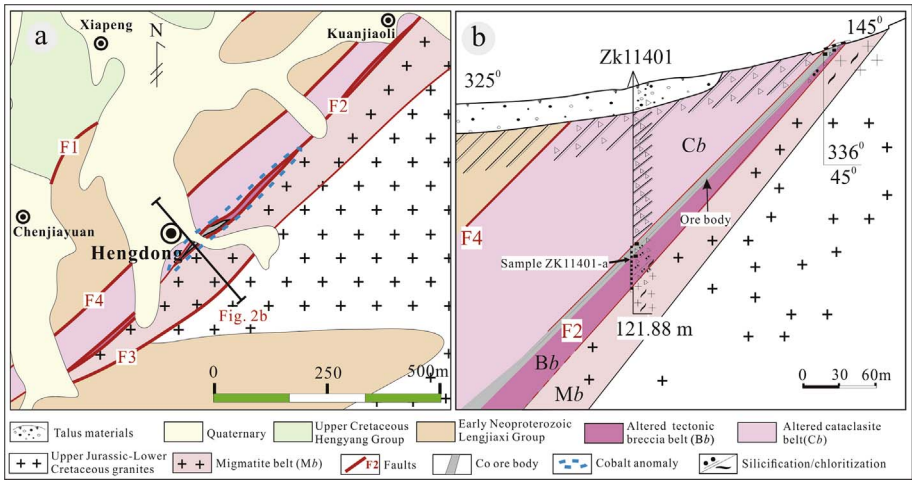

Fig. 2. (a) Geological map of the Hengdong Co deposit; (b) The No. 11401 drill profile of the Hengdong deposit.

Lengjiaxi Group (Fig. 2). The Cretaceous Hengyang Group consists of yellow-brown sandstone and some terrigenous sediments, which were deposited in the northeastern part of the Changsha-Pingjiang graben basin (Fig. 1b). The Lengjiaxi Group in the area is featured by a suite of flysch turbidites mainly composed of dark green sandstone, siltstone, pelitic siltstone, slate, and phyllite intercalated with volcanic rocks (Xu et al., 2007). The Co orebodies have been discovered predominantly within the altered (strong silicification and chloritization) tectonic breccia belt (B*b*) along F_2 (Fig. 2), and subordinately by migmatizated slates of the Lengjiaxi Group. Cobalt orebodies are mainly present as stratiform, stratiform-like or lensoid shapes and have a length of ~230 m and a width of ~15 m (Fig. 2). Wall rock alteration is dominated by zoned alteration with predominant silicification and chloritization proximal to the orebodies, and sericitization and carbonatization distal from the mineralization, as well as some localized carbonate alteration. There are two kinds of ore types in the Hengdong deposit: altered tectonic breccia and silicified rocks, with both showing similar mineral assemblages and alteration styles, despite a higher Co grade identified in the former ore type. The first type developed preferentially within the fault zones, which are commonly featured by euhedral to anhedral granular, cataclastic and metasomatic textures, and massive, disseminated, brecciated, nodular and vein/veinlet structures. The second ore type commonly appears at top of migmatites and is composed of quartz and disseminated pyrite.

4. Samples and analytical methods

Eighty-two samples were collected from the drilling-hole cores ZK11401, ZK11402, ZK501 and ZK1102 in the Hengdong deposit. All of these samples were prepared as polished thin section and examined by transmitted- and reflected light microscopy.

4.1. ^{40}Ar–^{39}Ar dating

To constrain the timing of both the reactivation of the CPDFZ and the Co mineralization, muscovite form two samples were date by ^{40}Ar–^{39}Ar method. Sample DY–003, mainly consisting of quartz (60%) and muscovite (35%), was collected from the mylonitic zone as part of the CPDFZ between the C*b* and the Liangyunshan pluton in the Hengdong district. Sample ZK11401-a was from the altered cataclasite-type ores, which mainly comprise quartz (ca. 80%), sulfides (10%), and muscovite (< 5%). The locations of samples DY–003 and ZK11401-a are shown in Figs. 1b and 2b, respectively. The selected samples were crushed into 60–80 mesh and then, muscovites were hand-picked under a binocular microscope and cleaned in an ultrasonic bath with deionized water for 30 min. After purifying the mineral separates to 99%, the prepared muscovite samples and a monitor standard, biotite ZBH-25 (ca. 132.5 Ma), were irradiated for 25 h at the 49–2 reactor in the China Institute of Atomic Energy. After 3 months cooling, the sample was analyzed by the ^{40}Ar–^{39}Ar laser heating method, which was summarized by Qiu and Jiang (2007) and Qiu et al. (2010). The correction factors for the values were: $(^{39}Ar/^{37}Ar)_{Ca}$ = 0.000653, $(^{36}Ar/^{37}Ar)_{Ca}$ = 0.000271, and $(^{40}Ar/^{39}Ar)_{K}$ = 0.00703. The total decay constant for ^{40}K of Steiger and Jager (1977) was chosen. The $^{40}Ar/^{39}Ar$ results were calculated and plotted using the ArArCALC software (Koppers, 2002).

4.2. Electron microprobe analysis (EMPA)

After determining the mineral paragenetic sequences, representative polished thin sections were chosen for mineral chemical analysis, including chlorite and pyrite. The spot analyses and X-ray elemental mappings were performed by SHIMADZU EPMA-1720 electron microprobe equipped with four wavelength-dispersive spectrometers at the Key Laboratory of Metallogenic Prediction of Nonferrous Metals, Central South University, Chinese Ministry of Education. All the analytical points were determined using high contrast backscattered electron (BSE) images. Operating conditions for spot analyses include an accelerating voltage of 20 kV, electron beam current of 15 nA, beam diameter of 1–2 μm, peak count time of 20 s, and background time of 10 s.

4.3. Laser ablation-inductively coupled plasma-mass spectrometry (LA–ICP–MS)

Analyses of trace elements in pyrite were carried out using a NWR193 nm laser ablation system coupled with an Finnigan Element 2 ICP-MS at the National Research Center for Geoanalysis, Beijing. Helium was used as a carrier gas, and argon used as makeup gas. The laser beam was fired at 10 Hz with 80 wt% laser energy. Spot size was 35 μm in diameter. MASS1, NIST610 and NIST612 (USGS sulfide standard) were used as reference materials for external standard, and KL2G (one of silicate standards MPI-DING from Max Planck Institutes, Germany) as the monitor. Total acquisition time was 40 s, background time was 20 s. The following isotopes were analyzed: ^{34}S, ^{49}Ti, ^{51}V, ^{52}Cr, ^{55}Mn, ^{57}Fe, ^{59}Co, ^{60}Ni, ^{65}Cu, ^{66}Zn, ^{71}Ga, ^{72}Ge, ^{75}As, ^{82}Se, ^{96}Mo, ^{107}Ag, ^{111}Cd, ^{115}In, ^{118}Sn, ^{121}Sb, ^{122}Te, ^{137}Ba, ^{205}Tl, ^{208}Pb, and ^{209}Bi. The detailed processing procedures can be also seen in Hu et al. (2008).

4.4. Fluid inclusions

Microthermometric measurements were carried out on a Linkam MDS 600 Heating-Freezing System in Key Laboratory of Mineralogy and Metallogeny at Guangzhou Institute of Geochemistry (GIG). Before the measurement, the stage was calibrated using synthetic fluid inclusions

containing pure H_2O (ice melting and critical homogenization) and H_2O-CO_2 inclusions (CO_2 triple point). The estimated accuracy of temperature measurements are ± 0.1 °C between −100 °C and 25 °C, ± 1 °C between 25 °C and 400 °C. The heating rate was generally 0.2–5 °C/min during the process of fluid inclusion testing, but reduced to 0.1 °C/min near the freezing point, and 0.2–0.5 °C/min near the homogenization temperature to record the phase transformation process accurately. To avoid the inclusion decrepitation, the freezing experiments were firstly carried out. In addition, fluid inclusions in quartz trapped along the same growth zone or cluster, were interpreted as representing primary ore-forming fluids (Goldstein and. Reynolds, 1994). Vapor and solid compositions of individual fluid inclusions were measured using the LabRam HR800 laser Raman micro-spectroscopy. An Ar^+ ion laser operating at 44 mW was used to produce an excitation wavelength of 532 nm line. The scanning range of spectra was set between 100 and 4000 cm^{-1} with an accumulation time of 10 s for each scan. The spectral resolution was 0.65 cm^{-1}. The Raman shift of a monocrystalline silicon piece was measured to be 520.7 cm^{-1} before analyzing.

4.5. Sulfur and lead isotope analysis

Twelve representative sulfide ore samples from the major Co ore bodies were collected. After weathered surfaces and diagenetic veins were trimmed off, pyrite (n = 12) and chalcopyrite (n = 1) separates from both the altered tectonic breccia and silicified rock mineralized samples were hand-picked using a binocular microscope. The pure separates were subsequently crushed into small pieces and powdered with a rock mill into 0.5–2 mm in diameter for S and Pb isotopes analysis. The prepared sulfide separates were leached of soluble sulfates in a 10% NaCl solution and rinsed three times in deionized water, and then were dissolved in 3 N HCl. The acidified samples were filtered, and an excess of 1 M $BaCl_2$ was added to the filtrate to precipitate $BaSO_4$. Accurately weigh 0.1 mg $BaSO_4$ precipitate after rinsing, filtering and drying, and then combined with an excess of V_2O_5 and analyzed for its S-isotope composition in the State Key Laboratory of Biogeology and Environmental Geology at the China University of Geosciences-Wuhan. Sulfur isotope compositions are expressed in standard δ-notation as per mille (%) variation with respect to V-CDT, using the conventional delta ($\delta^{34}S$) notation. Sulfur isotope results have an analytical error of ~0.1% calculated from replicate analyses of samples and the laboratory standards NBS 127 (21.1%), IAEA SO-5 (0.49%) and IAEA SO-6 (−34.05%).

The lead isotopic analyses on four pyrite separates were performed using a GV Isoprobe-T thermal ionization mass spectrometer monitored by standard NBS981 at the Analytical Laboratory of the Beijing Research Institute of Uranium Geology, China. The analytical procedure involved dissolution of samples using HF and $HClO_4$ in crucibles, followed by basic anion exchange resin to purify Pb. Analytical results for the standard NBS981 are $^{206}Pb/^{204}Pb$ = 16.937 ± 0.002 (2σ), $^{207}Pb/^{204}Pb$ = 15.457 ± 0.002 (2σ) and $^{208}Pb/^{204}Pb$ = 36.611 ± 0.004 (2σ).

5. Results

5.1. Mineralogy and the paragenesis

Generally, the sulfide minerals are dominated by Co-bearing pyrite, with minor chalcopyrite, galena and sphalerite (Fig. 3a–e). Pyrite, with different size, occurs as disseminated euhedral to subhedral grains in altered tectonic breccia belt (Fig. 3a and e). In some cases, pyrite is fractured or brecciated, with the microfractures filled by other sulfide minerals (Figs. b and c). Chalcopyrite is normally intergrown with pyrite, galena and sphalerite (Fig. 3c). It also occurs as veins crosscutting the gangue minerals, with pyrite inclusions (Fig. 3d).

The gangue minerals mainly consist of quartz, muscovite and chlorite, with minor rutile, epidote, albite and calcite (Fig. 3f–i). Field investigation and thin-section observation discriminated four types of quartz: (1) mylonitized quartz which is subdivided into undulose extinction quartz (Q1-1) and ribbon quartz (Q1-2) (Fig. 3 h–i), (2) coarse-grained quartz (Q2) intergrown with sulfide minerals (Fig. 3h and j), (3) fine-grained quartz (Q3) (Fig. 3j and k), and (4) quartz or quartz-calcite veinlets (Q4) (Fig. 3l). Chlorite occurs either as mm-scale polycrystals (named as Chl-1, Fig. 3m and n), intergrown with quartz, pyrite, rutile and epidote or as veinlets (named as Chl-2, Fig. 3g and o), which cuts the early minerals but is cut across by the late calcite vein (Fig. 3g).

Combined with the crosscutting relationships of the ore veins, the mineral assemblages and textures discriminated four mineral paragenetic sequences formed during the rock-forming and hydrothermal progresses (Fig. 4). The host rock is defined by a mineral assemblage of mylonitized quartz, ductile deformed feldspar and mica fish, deformed in response to ductile shearing. Quartz in the host rock includes Q1-1 and Q1-2, and coexists with minor or no sulfide minerals (Fig. 3h and i). In addition, muscovite generally occurs around quartz grains, with minor dissemination a within silicate minerals (Fig. 3f and i). The hydrothermal process is divided into three mineralization stages: the early-stage (E-stage), the middle-stage (M–stage) and the late-stage (L-stage) (Fig. 4). E-stage is characteristic of mineral assemblage quartz + pyrite + muscovite ± chalcopyrite, with quartz generally occurring as Q2 type and coexistent with coarse-grained, euhedral, disseminated pyrite as well as chalcopyrite (Fig. 3d and e). Pyrite in this stage is the main Co-bearing ore mineral and occurs as xenomorphic to subhedral microcrystal aggregates. M–stage is characterized by quartz + pyrite ± polymetallic sulfides, with quartz present as Q3-type and typically intergrown with fine- to medium-grained disseminated pyrite as well as minor pyrrhotite, chalcopyrite, galena and sphalerite (Fig. 3b and c). Other gangue minerals formed at this stage include chlorite (i.e. Chl-1), rutile and sericite, which are closely associated with sulfides (Fig. 3m and n). With minor pyrite, the L-stage has the main mineral assemblage of quartz, chlorite (i.e. Chl-2) and calcite, and generally formed as veinlets crosscutting the earlier minerals (Fig. 3g, l and o). Quartz in this stage mainly occurs as Q3 and Q4 type, but it is often intergrown with calcite (Fig. 3l).

5.2. ^{40}Ar–^{39}Ar ages

The ^{40}Ar–^{39}Ar dating data on muscovite separates from samples DY–003 and ZK11401–02 are presented in Table 1. Both samples yield well-defined age plateau, composed of at least three successive steps that account for more than 60% of the total ^{39}Ar released (Fig. 5). These continuous heating steps have apparent ages reproducible at the 95% confidence level, giving the plateau ages of 130.3 ± 1.4 Ma (MSDW = 0.90) for muscovite in sample DY-003 within the CPDFZ (Fig. 5a), and 124.7 ± 0.6 Ma (MSDW = 0.49) for muscovite in ore sample ZK11402-a (Fig. 5c), respectively. Correspondingly, the isochron ages of 127.9 ± 5.9 Ma (Fig. 5b) and 124.8 ± 0.7 Ma (Fig. 5d) for samples DY-003 and ZK11402-a, respectively are in good agreement with their plateau ages. The isochron (Fig. 5b and d) or inverse isochron plots (not shown) have $^{40}Ar/^{36}Ar$ ratios within error of the accepted value of the present air (298.56 ± 0.31; Renne et al., 2009). With together the air-like $^{40}Ar/^{36}Ar$ ratios, the well-defined plateau ages, reproducibility of the plateau and isochron or inverse isochron ages suggest that the radiogenic and nucleogenic gas fractions of the analyzed muscovite are hosted in tight reservoirs that remained closed and uncontaminated throughout their history (Li et al., 2012b).

5.3. Chlorite chemical composition

EPMA chemical analyses on the two groups of chlorite (i.e. Chl-1, Chl-2) are listed in Table 2, Appendix A1 and plot in Fig. 6. Table 2 shows that the concentrations of CaO, K_2O and Na_2O in both groups of chlorite are also relatively lower than that of other major oxides. Chl-1

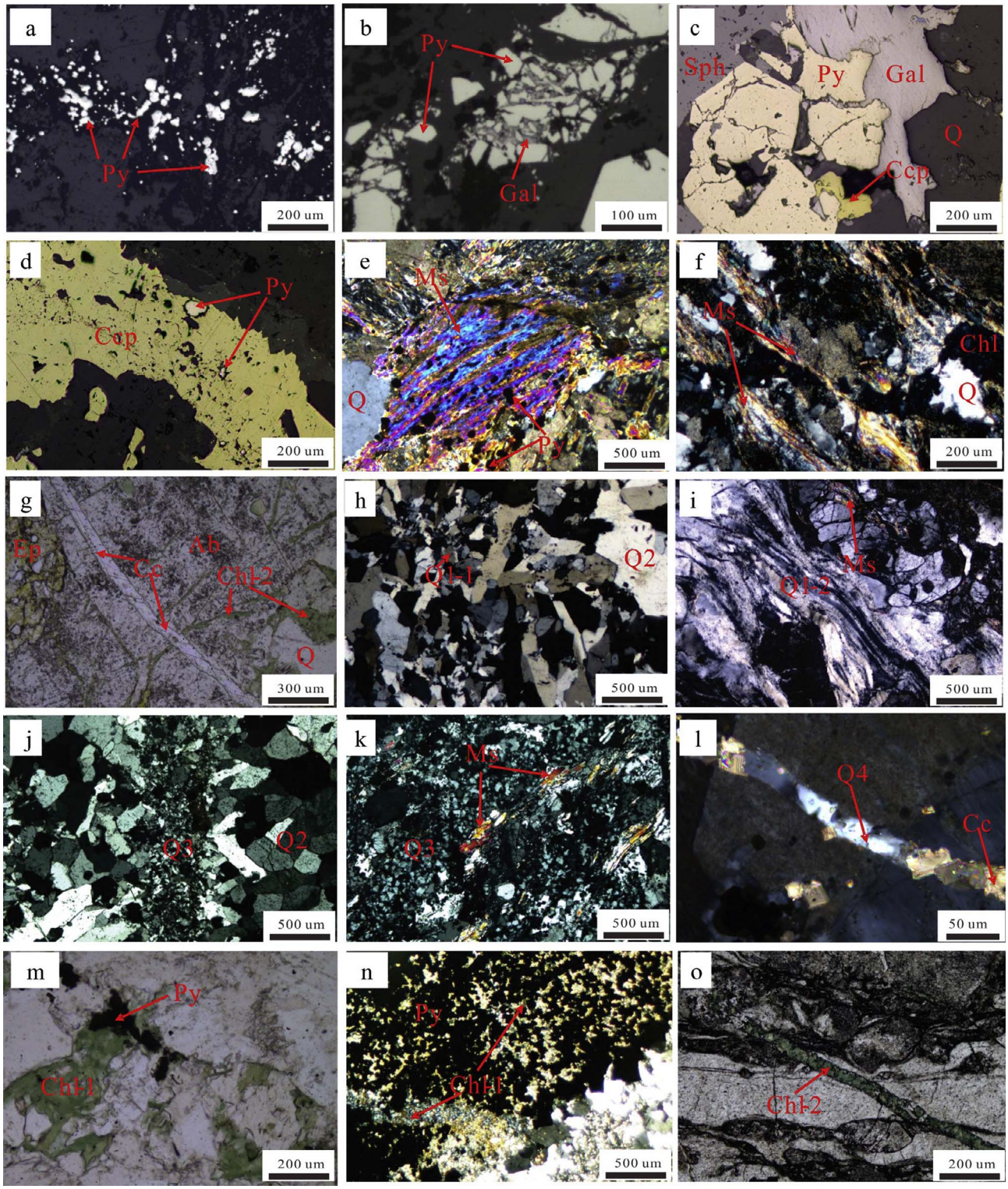

Fig. 3. Photographs showing composition and texture of the typical mineral assemblages in the Hengdong deposit. (a) disseminated euhedral to subhedral pyrite grains in altered tectonic breccia belt; (b) fractured pyrite, the microfractures filled with galena; (c) pyrite intergrown with chalcopyrite, galena, sphalerite and quartz; (d) pyrite as inclusion trapped in the chalcopyrite vein; (e) sample ZK11401-a, pyrite occurs as inclusion in the muscovite mineral, indicating that the precipitated at the same time; (f) muscovite occurs around quartz grains, with minor disseminations within silicate minerals; (g) chlorite cuts the early minerals but is crosscut by the late calcite vein; (h) undulose extinction quartz and the coarse grain quartz; (i) ribbon quartz with minor muscovite in wall rock; (j) the fine grain quartz crosscut the coarse grain quartz; (k) fine grain quartz with minor muscovite; (l) quartz-calcite vein cut the earlier minerals; (m) chlorite, intergrown with the pyrite, occurs either as mm-scale polycrystal; (n) chlorite intergrown with the disseminated pyrite; (o) chlorite vein crosscut the early minerals. Py = pyrite, Gal = galena, Sph = sphalerite, Ccp = chalcopyrite, Ms = Muscovite, Q = quartz, Q1-1 = quartz with undulose extinction, Q1-2 = ribbon quartz, Q2 = coarse grain quartz, Q3 = fine grain quartz, Q4 = quartz as vein intergrown with calcite, Chl = chlorite, Chl-1 = polycrystal chlorite, Chl-2 = vein chlorite, Ep = epidote, Ab = albite.

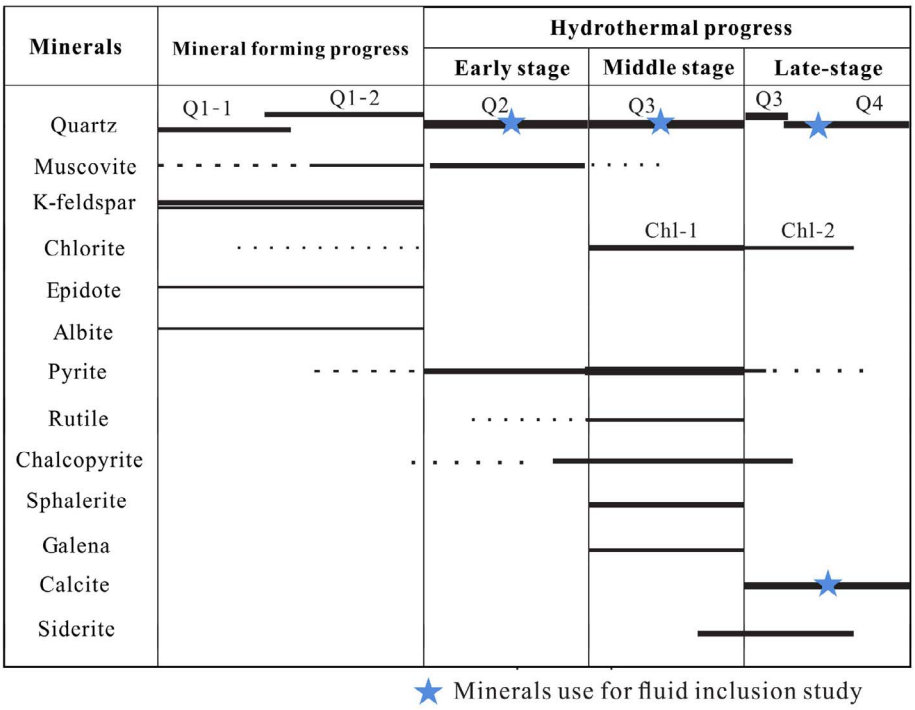

Fig. 4. Paragenetic sequence of the hydrothermal mineral assemblages in the Hengdong deposit. The widths of the solid lines denote the relative abundance of minerals.

shows a higher FeO contents than Chl-2, at a given MgO content (Fig. 6a). Moreover, the Chl-1 has lower concentrations in SiO_2 (21.3–25.3 wt%) and TiO_2 (0–0.064 wt%) but higher contents in Al_2O_3 (17.1–19.8 wt%), FeO (31.5–35.0 wt%), CoO (0–0.12 wt%) and MnO (0.4–0.7 wt%), relative to the Chl-2. The chlorite structure formulas were calculated by the Windows program (WinCcac) proposed by Yavuz et al. (2015). The results show that chlorite from the Hengdong Co deposit belongs to type-I category (i.e., Fe-rich and Mg-poor; Zane and Weiss, 1998). In addition, there are pronounced negative correlations of MgO with FeO and (FeO + MgO) with Al^{VI} for both the groups

Table 1
^{39}Ar–^{40}Ar isotopic data and ages of muscovite from Hengdong deposit and CPDFZ.

Run ID	$^{40}Ar/^{39}Ar$	$^{37}Ar/^{39}Ar$	$^{36}Ar/^{39}Ar$	$^{40}Ar^*/^{39}Ar$	$^{40}Ar^*$(%)	$^{39}Ar_K$(%)	Ag (Ma)	± 2σ (Ma)
Sample number = DY003; mineral = Muscovite; J value = 0.004871								
Step 1	15.908	0.857	0.022	9.338	58.66	7.71	80.25	5.12
Step 2	16.544	0.699	0.011	13.315	80.47	10.57	113.37	3.24
Step 3	18.362	0.590	0.021	12.345	67.21	8.83	105.34	4.16
Step 4	18.039	0.197	0.012	14.563	80.72	10.61	123.64	2.8
Step 5	17.367	0.0534	0.005	15.777	90.84	11.93	131.57	1.69
Step 6	15.995	-0.002	0.002	15.359	96.02	12.62	130.16	0.81
Step 7	15.726	0.094	0.001	15.311	97.35	12.79	129.76	1.39
Step 8	16.106	0.136	0.003	15.314	95.2	12.51	129.92	1.94
Step 9	16.304	0.045	0.003	15.373	94.6	12.43	130.7	1.15
Sample number = ZK11401-a; mineral = Muscovite; J value = 0.00897160								
16WHA-02	9.594	0.002	0.006	7.688	575.92	0.74	120.61	0.82
16WHA-03	8.629	0.001	0.003	7.829	3473.53	4.99	122.76	0.52
16WHA-04	8.404	0.000	0.002	7.816	5264.83	7.77	122.55	0.50
16WHA-05	8.430	0.000	0.002	7.840	2598.77	3.82	122.92	0.50
16WHA-06	8.394	-0.001	0.001	7.960	1907.59	2.82	124.73	0.54
16WHA-07	8.337	0.000	0.001	7.939	2231.16	3.32	124.42	0.57
16WHA-09	8.413	0.001	0.002	7.965	1763.14	2.60	124.81	0.52
16WHA-10	8.398	-0.001	0.002	7.948	1542.09	2.28	124.56	0.60
16WHA-11	8.462	0.000	0.002	7.951	4511.12	6.61	124.61	0.50
16WHA-12	8.432	0.000	0.002	7.945	5241.22	7.71	124.50	0.50
16WHA-13	8.439	0.000	0.002	7.958	4254.65	6.25	124.70	0.50
16WHA-14	8.367	0.000	0.001	7.961	4489.32	6.65	124.76	0.50
16WHA-16	8.365	0.000	0.001	7.959	4517.89	6.70	124.72	0.50
16WHA-17	8.330	0.000	0.001	7.972	4232.31	6.30	124.91	0.50
16WHA-18	8.306	-0.001	0.001	7.977	3453.34	5.16	124.99	0.50
16WHA-19	8.292	0.000	0.001	7.976	4587.65	6.86	124.97	0.50
16WHA-20	8.203	-0.001	0.001	7.945	4238.99	6.41	124.50	0.49
16WHA-24	8.149	0.000	0.001	7.976	7495.54	11.41	124.97	0.49
16WHA-25	8.061	0.002	0.000	7.965	855.16	1.32	124.81	0.51
16WHA-26	8.106	0.000	0.001	7.953	194.02	0.30	124.63	0.94

Note: The terms $^{40}Ar^*$ and $^{39}Ar_K$ denote radiogenic ^{40}Ar and nucleogenic ^{39}Ar, respectively.

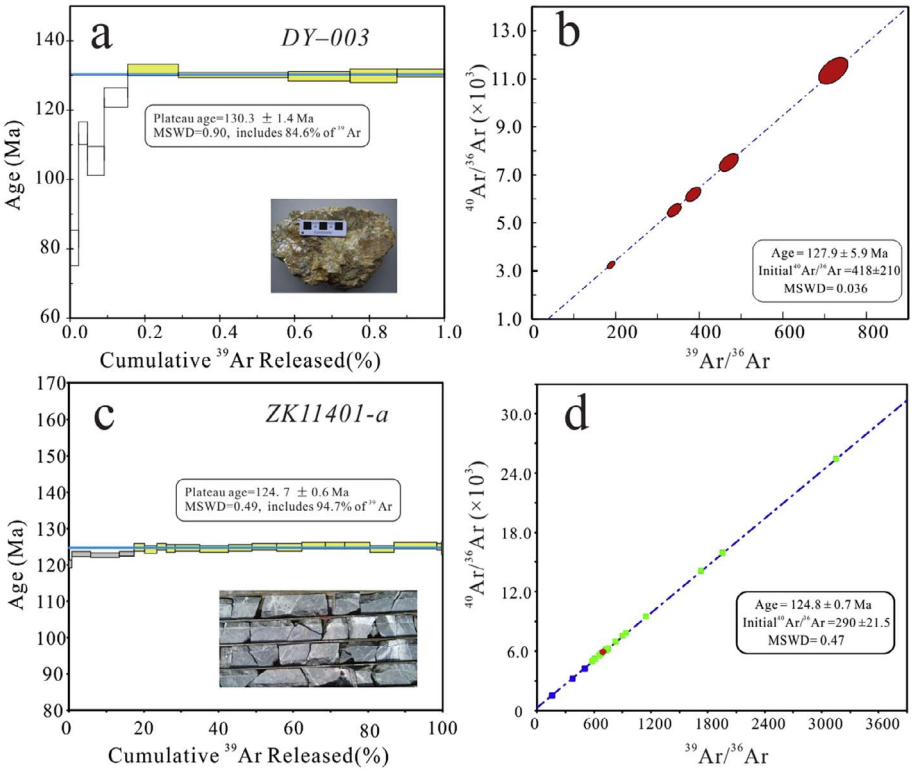

Fig. 5. ^{40}Ar–^{39}Ar age spectrum of muscovite separates extracted respectively from the Changsha-Pingxiang deep fault zone(CPDFZ) (a–b) and the ores in the Hengdong deposit (c–d).

Table 2
Chemical compositions (wt%) of chlorite from Hengdong deposit analyzed by EPMA, along with their structural formulae and estimated formation temperatures.

	Chl-1			Chl-2		
	Max	Min	Average	Max	Min	Average
SiO_2	25.33	21.29	23.15	28.27	24.56	25.91
TiO_2	0.06	0.00	0.03	0.41	0.00	0.06
Al_2O_3	19.80	17.69	18.76	19.86	15.61	18.02
FeO	35.04	31.49	33.33	34.88	29.96	33.06
MnO	0.70	0.41	0.55	0.52	0.33	0.41
MgO	13.06	9.71	11.41	13.75	8.92	10.41
CaO	0.11	0.01	0.03	0.11	0.00	0.03
Na_2O	0.03	0.00	0.01	0.09	0.00	0.02
K_2O	0.07	0.00	0.01	0.30	0.01	0.08
CoO	0.12	0.00	0.05	0.00	0.00	0.00
Total	89.39	83.83	87.33	89.29	86.97	88.02
Si^{IV}	2.75	2.45	2.59	3.06	2.74	2.85
Al^{IV}	1.55	1.25	1.41	1.26	0.94	1.15
T site	4.00	4.00	4.00	4.00	4.00	4.00
Al^{VI}	1.22	0.93	1.07	1.31	1.01	1.18
Ti	0.01	0.00	0.00	0.03	0.00	0.00
Fe^{+2}	3.36	2.93	3.13	3.24	2.71	3.04
Mn	0.07	0.04	0.05	0.05	0.03	0.04
Mg	2.16	1.64	1.91	2.21	1.46	1.70
Ca	0.01	0.00	0.00	0.01	0.00	0.00
Na	0.01	0.00	0.00	0.02	0.00	0.00
K	0.01	0.00	0.00	0.04	0.00	0.01
Cations	10.28	10.01	10.16	10.03	9.82	9.99
Octahedral vacant	0.00	0.00	0.00	0.20	0.00	0.03
Fe/(Fe + Mg)	0.67	0.57	0.62	0.69	0.55	0.64
Mg/(Fe + Mg)	0.43	0.33	0.38	0.45	0.31	0.36
Battaglia-1999	286	245	264	250	206	234
Zang-1995	318	253	290	256	187	234
Cathelineau-1985	347	282	316	286	218	262
Average	317	260	290	264	204	243

Notes: Total iron content as FeO. Temperatures of chlorite formation were calculated based on the geothermometers of Battaglia (1999), Zang and Fyfe (1995) and Cathelineau and Nieva (1985), respectively. Min = minimum, Max = maximum.

of chlorite (Fig. 6a and b). Nevertheless, a better correlation (R^2 = 0.94) accounting for the Chl-1 (Fig. 6b) indicates that the substitution vector, $3(Mg, Fe^{2+})^{VI} = \square + 2(Al^{3+})^{VI}$, is more efficient in the M-stage ($\square$ denotes the octahedral site vacancy). The structural calculation also shows that Chl-1 has ranges of Si: 2.45–2.75 apfu, Fe: 2.93–3.36 apfu, R^{2+} (Mg + Fe + Mn): 4.79–5.33 apfu, and Fe/$(Fe + Mg)_{mol}$: 0.57–0.67. In contrast, Chl-2 has ranges of Si: 2.74–3.06 apfu, Fe: 2.71–3.24 apfu, R^{2+} (Mg + Fe + Mn): 4.45–4.97 apfu, and Fe/$(Fe + Mg)_{mol}$: 0.55–0.69. The chemical composition of chlorite from the Hengdong Co deposit falls in brunsvigite to pseudothuringite fields (Fig. 6c). The classification of Wiewióra and Weiss (1990) based on the chlorite structure differences shows that Chl-1 falls in the Sheridanite-Ripidolite field, whereas Chl-2 plots in the Clinochlore-Chamosite field (Fig. 6d), and that the octahedral site in Chl-1 are occupied by R^{2+}. This result is also shown in Fig. 6e, which suggests that the Al^{IV}/Al^{VI} ratios in Chl-1 are around 1.0 and that the Chl-2 have more tetrahedral Al than octahedral Al.

Generally, the octahedral vacancy sites of chlorite are occupied by Na^+, K^+ and Ca^{2+}. This octahedral vacancy site, may be responsible for the existence of mica or smectite layers or inclusion, is absent in Chl-1 but appears in Chl-2. However, the low total alkali ($Na_2O + K_2O + CaO$) contents (< 0.5 wt%) and Ca values of less than 0.10 apfu in chlorite analyses from the Hengdong ores suggest the absence of smectite and/or illite intergrowths within chlorite flakes (Cathelineau and Nieva, 1985). This indicates the presence of complete stoichiometry and suitability for thermometry studies. That is, empirical geothermometers of chlorite can be suitable for samples of the Hengdong deposit for estimating temperature of formation of hydrothermal chlorite and associated mineralization. The empirical chlorite geothermometers are based on either the interplanar spacings d_{001} or the variation of Al^{IV} values or the amount of octahedral vacancies or the Fe/(Fe + Mg) ratios of chlorites as a function of temperature (Cathelineau and Nieva, 1985; Zang and Fyfe, 1995; Battaglia, 1999). Some authors also have expressed view that the above parameters may have been influenced by the fluid/ rock interaction ratio, oxygen and sulfur fugacities, and pH in the hydrothermal fluid (Klein et al., 2007

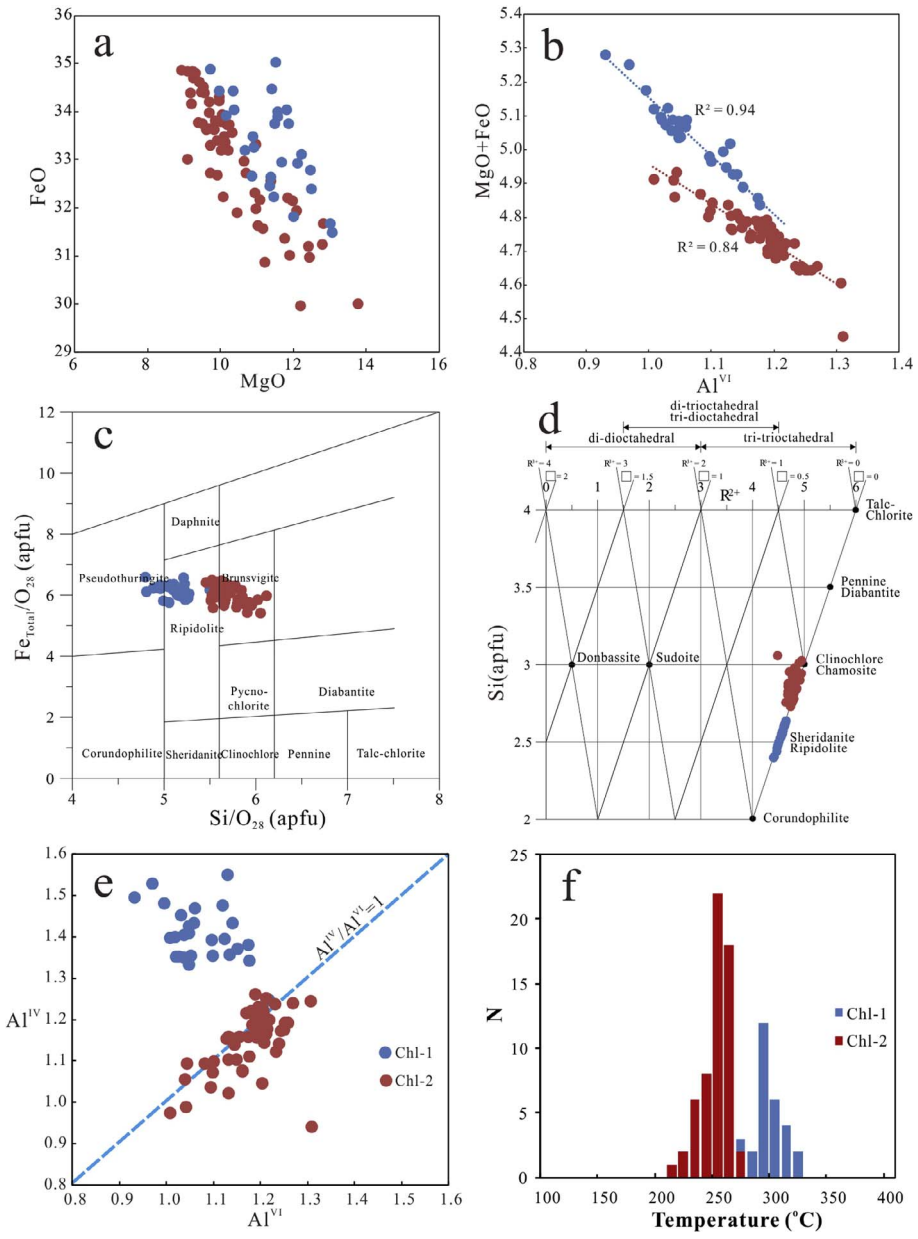

Fig. 6. Showing chlorite chemical compositions (a–b), classification (c–d) and calculated temperatures (f). (a) MgO vs. FeO diagram of chlorite; (b) Plot of Al^{VI} contents vs. Mg + Fe contents of chlorite; (c) Plot of Fe vs. Si, (after Deer et al., 1992); (d) Plot of chlorites in R^{2+} vs. Si diagram (after Wiewióra and Weiss, 1990); (e) Al^{IV} vs. Al^{VI} diagram of chlorite; (f) Calculated temperatures for chlorite formation based on average value of different chlorite geothermometer (see: Table 3 for details). Chl-1 and Chl-2 are from the M- and L- stages of mineralization, respectively.

and references therein). Even so, the basic principles are still observed in this study, e.g., good correlation between the Fe + Mg value to Al ^{IV} contents (Fig. 6b), the value of Ca + Na + K < 0.5 apfu (Appendix A1). Thus, three empirical methods (Cathelineau and Nieva, 1985; Zang and Fyfe, 1995; Battaglia, 1999), yielding the distinguishing temperatures from the M- and L-stage, were chosen to constrain the chlorite-forming temperatures. The estimated temperatures from the three geothermometers (Table 2) show that the highest temperature obtained from Cathelineau and Nieva (1985), but the lowest temperature is derived from Battaglia (1999). Ultimately, the average temperature based on the different four methods were considered as the chlorite-forming temperature because of the bias of each empirical method. The integration of the four empirical methods ultimately confirms the forming temperatures of Chl-1 and Chl-2 at ~280–350 °C and ~120–290 °C, respectively (Fig. 6f and Table 2).

5.4. Pyrite chemical composition

Thirty-four LA–ICP–MS analyses on trace elements of pyrite from the Hengdong district are given in Table 3 and Appendix A2, including 14 pyrite grains and 20 pyrite grains from the M-stage and the wall rock, respectively. The pyrite grains in the E- and L-stages are so small and easy to contaminate with other kinds of minerals during laser ablation. Therefore, only the data obtained from the wall rock and the M-stage pyrite are discussed. In this study, to avoid the effects of micron sized inclusions, the inclusion free (under the microscope) pyrites were chosen for LA–ICP–MS analyses. However, the invisible or nano-sized inclusions may still influence the results. From the representative time-resolved depth profiles for pyrite (Fig. 7a and b), Co are flat and abundant in the two types of pyrite, the parallel trends of smooth or spiky pattern between Fe and Co support the close correlation of their concentrations, which is consistent with the EMPA mapping results (Fig. 7c and d). Cobalt is the most abundant trace element in pyrite in the Hengdong deposit (Fig. 8), Co concentrations varying from 70.5 ppm to 10596 ppm (1383.8 ± 2219 ppm) in the wall rock pyrite and 878 to 8609 ppm (4120 ± 2740 ppm) in the M-stage pyrite. Fig. 8 reveals that two types of pyrite contain higher Ni, As and Se, and they have a narrow distribution. Measured values for Pb and Bi vary over several orders of magnitude, from under detection limits to tens ppm (Table 3 and Fig. 8), which may result from the attribution of

Table 3
The trace elements range of pyrite in M-stage and wall-rocks from the Hengdong deposit.

No.	M-stage				Wall rock			
	Max	Min	Average	STDEV	Max	Min	Average	STDEV
Cu	11.59	0.01	4.64	3.67	8.80	0.00	3.35	2.39
Sc	0.28	< bdl	0.11	0.10	0.61	< bdl	0.22	0.16
V	0.09	< bdl	0.05	0.03	5.54	< bdl	1.40	1.84
Cr	3.34	< bdl	1.57	1.24	7.00	< bdl	1.97	1.82
Mn	2.45	1.02	1.58	0.43	78.07	1.01	15.13	21.43
Co	8609.00	878.10	4119.79	2740.81	10596.00	70.54	1383.85	2219.24
Ni	263.50	23.59	111.41	77.53	271.80	12.38	75.59	65.90
Zn	18.27	2.03	5.79	5.01	9.26	3.03	5.18	1.56
Ga	0.08	< bdl	0.04	0.03	1.53	< bdl	0.45	0.53
Ge	3.73	0.94	2.14	0.88	3.40	0.32	2.25	0.80
As	1532.00	136.10	633.14	420.40	1549.00	75.32	671.73	467.51
Se	151.30	41.17	86.08	33.57	161.50	30.65	87.08	32.94
Mo	4.13	2.75	3.36	0.43	6.25	2.68	4.05	0.79
Ag	1.15	< bdl	0.35	0.41	0.70	< bdl	0.41	0.16
Cd	0.20	< bdl	0.09	0.08	0.27	< bdl	0.11	0.08
In	0.03	< bdl	0.02	0.01	0.03	< bdl	0.01	0.01
Sn	0.33	< bdl	0.14	0.12	0.50	< bdl	0.19	0.14
Sb	1.87	< bdl	0.65	0.77	0.41	< bdl	0.14	0.13
Te	0.81	0.06	0.33	0.20	1.13	< bdl	0.37	0.29
Cs	0.11	< bdl	0.05	0.04	0.05	< bdl	0.03	0.02
Ba	0.48	< bdl	0.12	0.16	5.94	< bdl	0.71	1.55
Au	0.07	< bdl	0.03	0.02	0.06	< bdl	0.02	0.02
Tl	0.19	< bdl	0.06	0.07	0.03	< bdl	0.02	0.01
Pb	33.89	0.04	8.77	12.71	14.02	< bdl	5.78	5.09
Bi	64.39	< bdl	13.56	22.01	34.80	< bdl	12.36	11.99
Co/Ni	86.16	14.96	41.75	23.44	334.26	1.20	31.17	70.46

Note: bdl: below detection limit. STDEV: standard deviation.

microscopic inclusions. The concentrations of Cu, Co, Ni, Ag, Au and Sb in the M-stage pyrite are generally higher than those in the wall rock pyrite (Fig. 8), whereas the concentrations of Sc, V, Mn, Ga, Cd and Ba are higher in the wall-rock pyrite, and these elements are also show a larger variation in the wall-rock pyrite (Fig. 8). The element patterns indicate that these elements are either influence by the inclusions or the

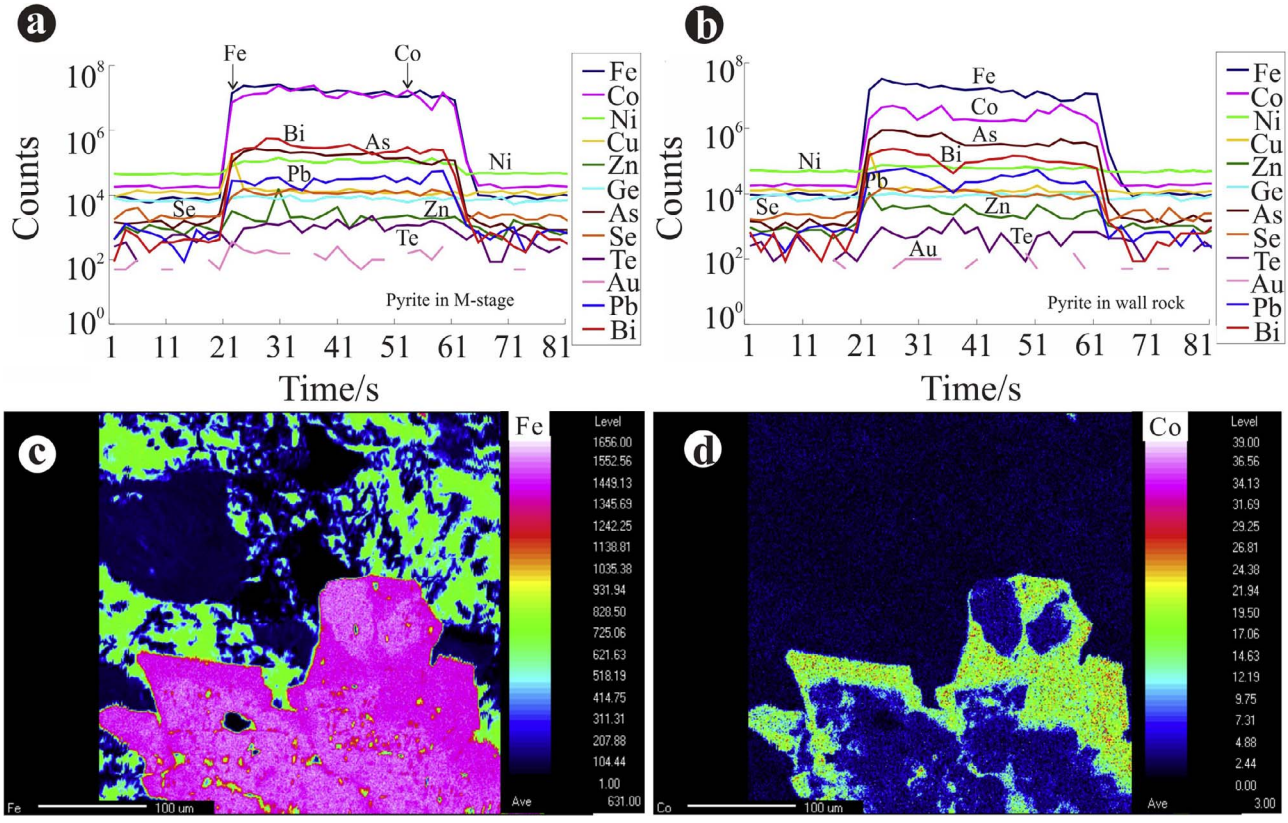

Fig. 7. (a and b) selected trace elements in pyrite from the Hengdong deposits for the LA-ICPMS ablation time-resolved depth profiles; (c and d) EPMA compositional maps showing textures and Fe and Co compositional variation.

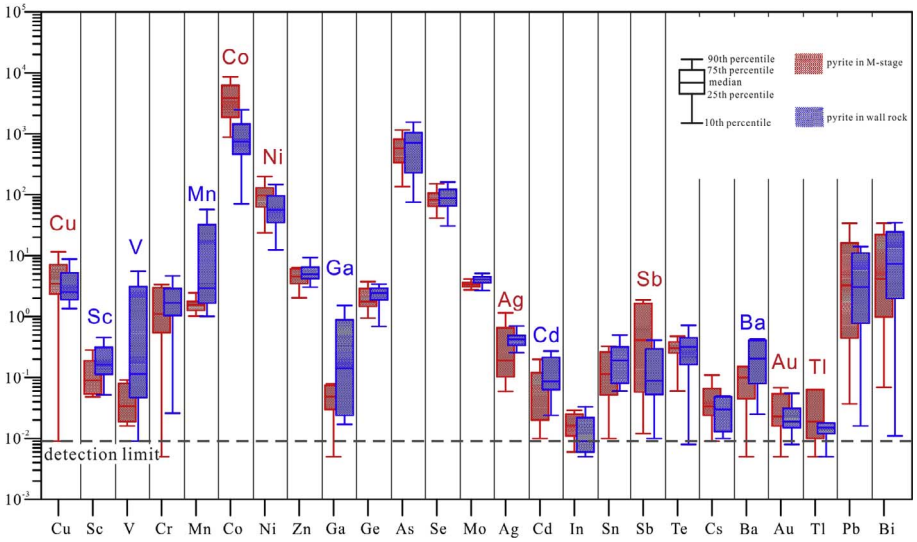

Fig. 8. Distribution of trace element in wall rock pyrite and M-stage pyrite.

mobility of themselves. The other elements, like In, Sn, Te, Cs, Au and Tl, in most of pyrite samples are near the detection limits (Fig. 8) and show a narrow variation, although some elements can as high as tens ppm. The Co/Ni ratios in the two types of pyrite are higher than 1, but in the wall-rock pyrite are more variable than that in the M-stage pyrite (Table 3).

5.5. Fluid inclusions

5.5.1. Fluid inclusion types

To characterize the nature and composition of the ore fluids, 48 doubly polished thin sections (about 0.20 mm thick) were collected from the different mineralized stages for fluid inclusion study. These samples consist of quartz or calcite and variable amount of pyrite, with or without minor other sulfides. Since the composition of fluid inclusion in this study is simple and we wish to uncover the evolution trends of the ore-forming fluids. For the present study, only different types of quartz and calcite were chosen, and the chronological relationships are based on the mineral paragenesis (Fig. 4). Detailed petrology mapping of fluid inclusions in quartz and calcite was undertaken to depict the fluid inclusion sizes, types, morphologies, vapor–liquid ratios and spatial clustering.

Fluid inclusion types are identified based on their phases (L-V-S) at room temperature (25 °C), phase transitions observed during heating and cooling (−196 to 600 °C), and Laser-Raman spectroscopy. Fluid inclusions in quartz or calcite from the different mineralization stages of Hengdong deposit mostly occur in clusters, with most inclusions showing elliptical forms and < 5–25 μm in size (Fig. 9). According to the rule of Roedder (1984), four types of primary or pseudosecondary fluid inclusions in quartz are determined (Table 4). These are, in decreasing order of abundance, liquid + vapor (LV), liquid + vapor + solid(s) (LVS), vapor-rich (V-rich) and pure liquid (PL) inclusions. The LV inclusions are common and contain two phases at room temperature, with most inclusions being liquid-rich (10–20 vol% vapor, Fig. 9c and e). Laser-Raman spectroscopy reveals that the vapor phase consists in the majority of inclusions of 100% H_2O with a few inclusions that contain traces (< 1 mol%) of CO_2. The liquid-rich three-phase LVS inclusions occur as negative crystal and elliptical shapes and contain several daughter minerals composed of halite, sylvite, sulfide and other unidentified daughter minerals (Fig. 9a and d). V-rich inclusions, contain a visible liquid phase and contain a visible of 65–90 vol% H_2O vapor, as determined by Laser-Raman spectroscopy. Generally, V-rich inclusions have random distribution and sometimes coexists with the LV fluid inclusions (Fig. 9f and g). The PL inclusions are rare and most of them have a linear arrangement, except for those locally occurring as clusters (Fig. 9b).

5.5.2. Microthermometry and salinity

The majority of fluid inclusions show initial ice melting temperatures (T_i) ranging from -27 °C to -21 °C (n = 34), with a clustering between −23 °C and −21 °C (n = 30), indicating that some of these inclusions contain, in addition to Na^+, other cations such as Mg^{2+} or Ca^{2+} in the liquid phase. Nevertheless, Potter et al. (1978) reveal that the P-V-T-X properties of brines in the system Na-K-Ca-Mg-CI-Br-SO_4-H_2O can be estimated to within ± 1.0% by the properties of an NaCl solution of the same final ice melting temperature. Therefore, the salinities in these inclusions were approximately estimated using the data for the NaCl–H_2O system of Bodnar (1994). Detailed microthermometry data are listed in Table 4 and shown in Fig. 10.

In the E-stage mineralization, LV- and V-rich inclusions as the most abundant types and a minor amount of LVS inclusions. The LV inclusions homogenized to liquid at 250.9–289.1 °C (Fig. 10a) and exhibit final ice melting temperatures from −10.9 to −5.9 °C, indicating salinities ranging from 9.08–14.87 wt% NaCl equiv. (Fig. 10d) and densities from 0.86–0.92 g/cm^3. The V-rich inclusions homogenized to vapor at 261.3–329.6 °C (Fig. 10a) and exhibit final ice melting temperature at −10.6 to −6.0 °C, indicating that their salinities range from 9.21 to 14.57 wt% NaCl equiv. (Fig. 10d) and densities from 0.80 to 0.88 g/cm^3. The LVS inclusions decrepitated while either the vapor bubble or some solids were still present, thus, no mircothermometric data are available for LVS inclusion. The M-stage fluid inclusions in quartz are dominated by LV and PL inclusions, with less abundant V-rich inclusions and LVS inclusions than E-stage. The LV inclusions exhibit final ice melting temperatures occur between −10.0 and −6.9 °C, equivalent to salinities of 10.36–13.94 wt%. The homogenization temperature of LV inclusions (to the liquid phase) shows temperature range from 216.6 to 289 °C, with the majority clustering between 240° and 280 °C and moral values around 270 °C (Fig. 10b). Bulk densities range from 0.86–0.93 g/cm^3. The V-rich inclusions show final ice melting temperatures, between −12.0 and −4.4 °C (Fig. 10e), resulting in salinities of 9.73–15.69 wt% NaCl equiv., which are higher than those from LV inclusions. The V-rich inclusions have homogenized temperature (to the vapor phase) from 257 °C to 365.4 °C (Fig. 10b), and contain bulk densities ranging from 0.76 to 0.87 g/cm^3. Heating experiments conducted on several of coexisting LV and V-rich inclusions, near the cores of quartz crystals, show that the LV and V-rich inclusions homogenized at the narrow range temperature (255–265 °C) into the different phases. LVS inclusions had a tendency to decrepitate prior to complete or partial homogenization, and the bubble disappear earlier than the solid phase, indicating the solid phase was trapped by

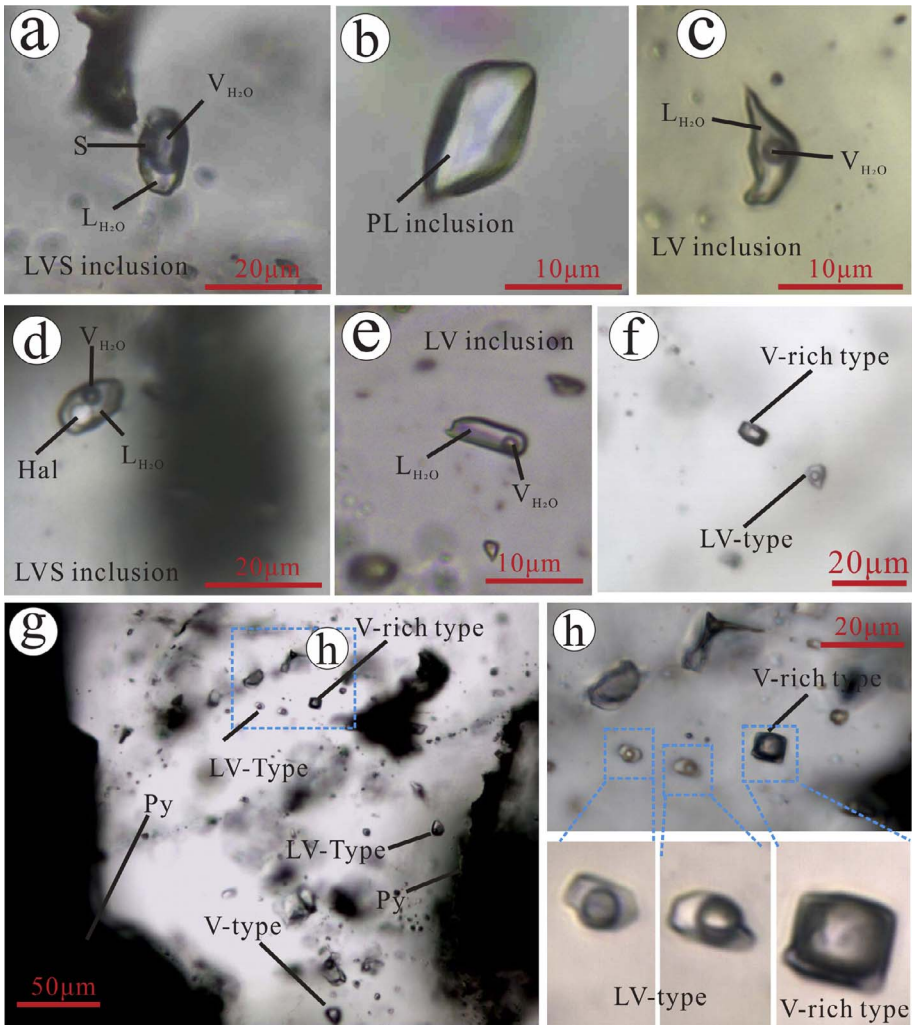

Fig. 9. Photographs showing the characteristics of fluid inclusions in quartz from the Hengdong ores. (a) LVS-type inclusions, the solid phase is halite; (b) E-stage, PL-type inclusions with V_{H2O} and L_{H2O}; (c) L-stage, LV inclusions; (d) M-stage, LVS-type inclusions with sub-transparent minerals; (e) M-stage, LV-type inclusions with V_{H2O} and L_{H2O}. (f) V-rich and L-type inclusions in M-stage; (g) M-stage, coexistence of V-rich and L-type inclusions; (h) V-rich and L-type inclusions in the field of (g). V_{H2O} = H_2O vapor; L_{H2O} = H_2O liquid; Hal = halite; Py = pyrite.

accident. Therefore, four LVS inclusions homogenized ranging from 275 °C to 387 °C are meaningless in the current discussion.

In the L-stage quartz, only LV inclusions with the small sizes of 2–5 μm were observed. The homogenization temperatures of this fluid inclusions type vary from 149.9 °C to 234 °C, the salinities from 9.6 to 16.0 wt% NaCl equiv. (Fig. 10c and f) and densities from 0.93 to 1.02 g/cm^3.

5.6. Sulfur and lead isotopes

Table 5 lists the sulfur isotopic data of one chalcopyrite and eleven pyrite separates. These sulfide separates yield large variation of $\delta^{34}S$ values, ranging from −1.5 to −15.9% (majorly between −7.5 and −15.9%) (Fig. 11). The lead isotopic compositions of pyrite and chalcopyrite separates are shown in Table 5. The $^{206}Pb/^{204}Pb$, $^{207}Pb/^{204}Pb$, and $^{208}Pb/^{204}Pb$ values of the Hengdong deposit vary from 18.156 to 18.761, 15.645 to 15.662, and 38.469 to 39.172, with averages of 18.319, 15.649, and 38.616, respectively. All lead isotope data plot close to the orogenic and lower crust lead and but higher than that of the modern mantle (Fig. 12).

6. Discussion

6.1. Timing of Co mineralization

Hydrothermal muscovite in the ore sample ZK11401–02 has clear petrographic relationship with Co mineralization (Fig. 3e). Therefore, the ^{40}Ar–^{39}Ar age of ca. 125 Ma (Fig. 6c and d) gives a direct constraint

Table 4
Microthermometric data of the fluid inclusions in quartz from the Hengdong deposit.

Stage	Type	Number	T_i (°C)	T_m (°C)	H_s	T_h (°C)	Salinity	Density
P-stage	LV	27	−23.3 to −21.3	−2.5 to −0.1	Liquid	169.0–223	0.18–4.18	0.85–0.93
E-stage	LV	19	−25.4 to −22.4	−10.9 to −5.9	Liquid	250.9–289.1	9.08–14.87	0.86–0.92
	V-rich	24	–	−10.6 to −6.0	Vapor	261.3–329.6	9.21–14.57	0.80–0.88
M−stage	LV	15	−25.0 to −21.0	−10.0 to −6.9	Liquid	216.6–289	10.36–13.94	0.86–0.93
	V-rich	18	−25.2 to −21.5	−12.0 to −4.4	Vapor	257–365.4	9.73–15.69	0.76–0.87
L-stage	LV	51	−22.8 to −21.2	−12.0 to −6.3	Liquid	149.9–234	9.60–15.96	0.93–1.02

Note: T_i (°C) = initial ice-melting temperature; T_m (°C) = final ice or solid melting temperatures; H_s = Homogenization state; T_h (°C) = final homogenization temperature; Salinity = wt% NaCl; Density = ρ (g/cm^3); – = No data has been obtained.

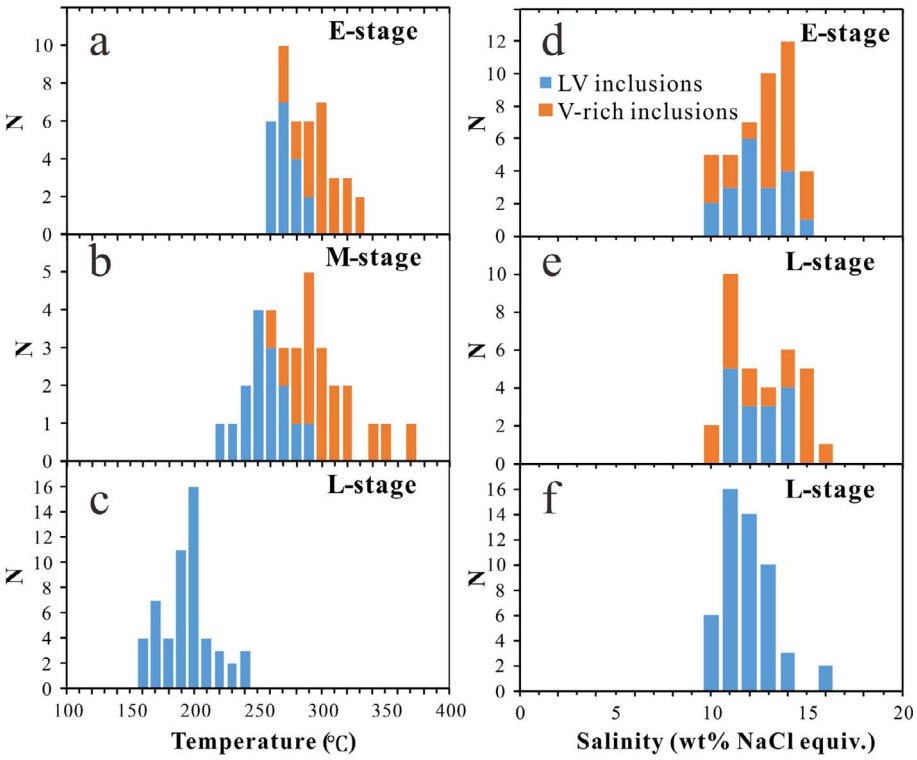

Fig. 10. Diagrams of homogenization temperature (a–c) and salinity (d–f) in different stages.

on the timing of Co mineralization. This age represents the time when the ore sample cooled below the closure temperature of argon isotopes in muscovite. As mentioned above, the ore temperatures of the Hengdong deposit defined by both the M-stage quartz fluid inclusion homogenization temperatures and hydrothermal chlorite, are lower or close to the mica argon closure temperature of 350 – 300 °C (McDougall and Harrison, 1999). Hence, the ca. 125 Ma age dated on the hydrothermal muscovite can be considered to represent the Co mineralizing age. The muscovite from the mylonitized sample within the CPDFZ yielded a well-developed, broadly consistent age of ca. 130–127 Ma (Fig. 6a and b), revealing that a pre-mineralizing event likely associated with the latest movements of the CPDFZ. The Lianyunshan pluton, to east of the Hengdong district, has an emplacement age of 145.17 ± 0.85 Ma (zircon U-Pb, Deng et al., 2017) and characterizes strong ductile shearing and mylonitization for its local outcrop near to the CPDFZ (Fig. 2b). To west of the district, the Wangxiang, Jinjing and Mufushan plutons also have muscovite ^{40}Ar–^{39}Ar plateau age of 146.9 ± 1.6 Ma (our unpublished data), LA–ICP–MS zircon U–Pb age of ca. 145 Ma (Deng et al., 2017), and zircon U-Pb ages of ca. 154–146 Ma (Wang et al., 2014), respectively. Therefore, the

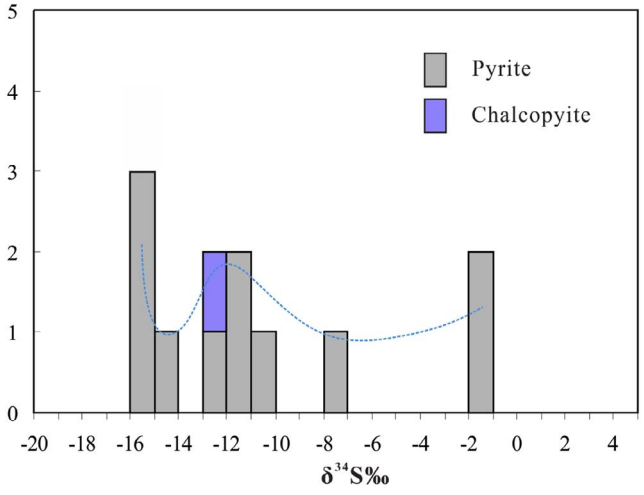

Fig. 11. Sulfur isotopic components of sulfide minerals in the Hengdong deposit.

Table 5
Sulfur and lead isotopic results of pyrite and chalcopyrite from Hengdong deposit.

Sample	Minerals	depth	$\delta^{34}S\%$(– CDT)	$^{206}Pb/^{204}Pb$	$^{207}Pb/^{204}Pb$	$^{208}Pb/^{204}Pb$
ZK11401-04	Pyrite	99.3 m	−15.3			
ZK11401-08	Pyrite	110.1 m	−12.8			
ZK11401-08	Chalcopyrite	110.1 m	−12.3			
ZK11401-06	Pyrite	99.3 m	−15.6			
ZK11401-05	Pyrite	101.2 m	−15.9			
ZK11401-03	Pyrite	96.8 m	−14.9			
ZK11401-02	Pyrite	94.1 m	−1.7			
ZK11401-02a	Pyrite	92.3 m	−1.5			
ZK11401-01	Pyrite	89.5 m	−15.1			
ZK1102-05	Pyrite	–	−10.1	18.156	15.645	38.469
ZK1102-04	Pyrite	–	−7.5	18.761	15.662	39.172
ZK1102-03-R	Pyrite	–	−11.6	18.187	15.650	38.531
ZK1102-03	Pyrite	–	−11.3	18.689	15.660	39.095

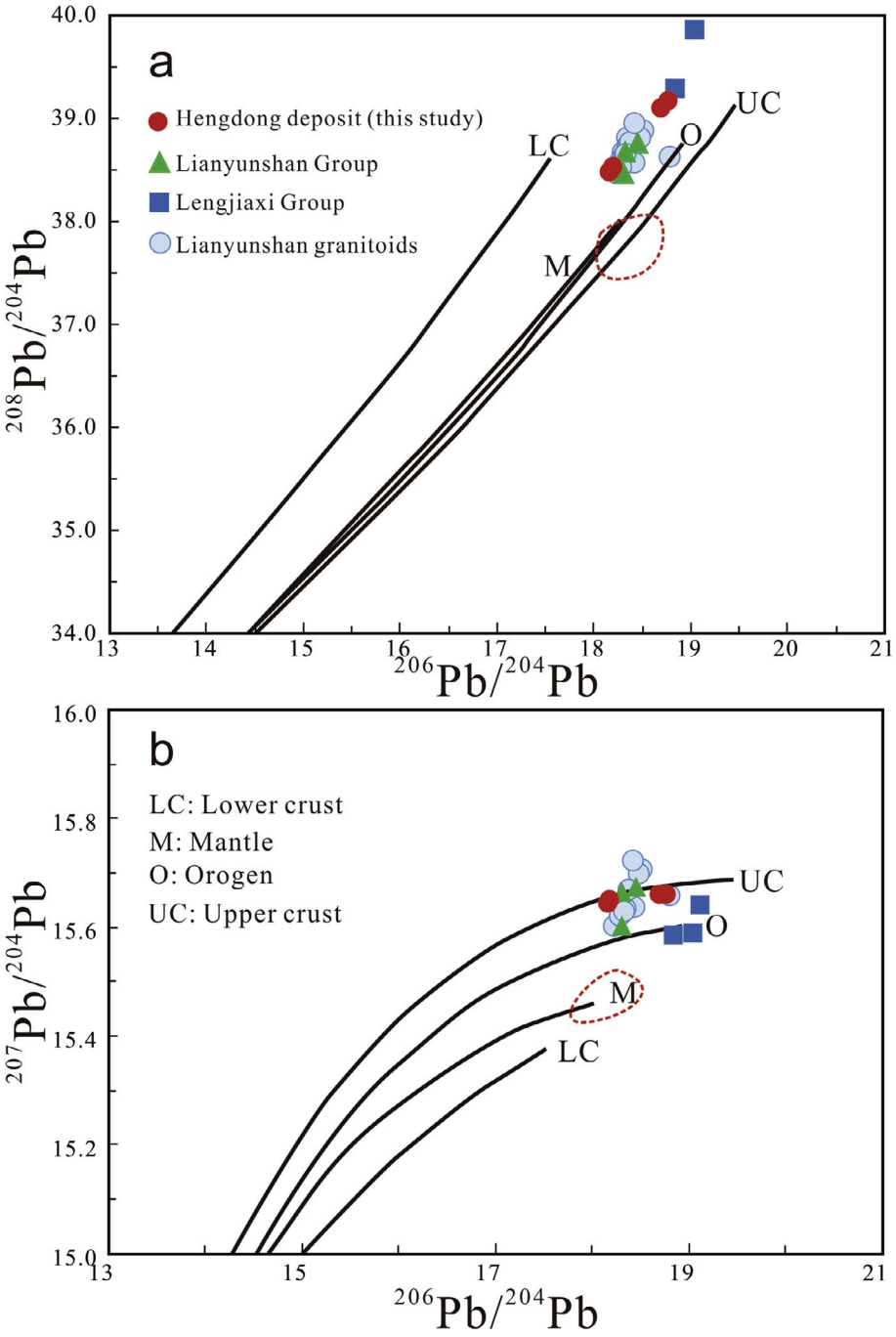

Fig. 12. Plots of lead ratios of the Hengdong deposit. The lead evolution curves of the upper crust, lower crust, mantle and orogen are from Zartman and Doe (1981). The red dashed lines enclose probable average modern composition of mantle (modified from Zartman and Haines, 1988). Lead isotope data of the Hengdong deposit are from this study, the Neoproterozoic Lengjiaxi Group from Liu et al. (1994), Lianyunshan Group and Lianyunshan Granitoids from Xu et al. (2009). (For interpretation of the references to colour in this figure legend, the reader is referred to the web version of this article.)

occurrence of the Hengdong Co mineralization is significantly younger than the emplacement of the late Jurassic to earliest early Cretaceous plutons but indicates a possible genetic link to the ductile-shearing and associated mylonitization in the northeastern Hunan Province. Moreover, this large time gap (ca. 30–20 Ma) between the Co mineralization and the plutons reveals a tenuous correlation of the ore-forming fluids with the magma-derived hydrothermal fluids, which is supported also by evidence from the following discussions.

The JOB of South China, which mainly contains low-grade metamorphic volcaniclastic and sedimentary rocks, was formed from the early Neoproterozoic assembly of the Yangtze and the Cathaysia blocks along the Jiangshan-Shaoxing fault (Li et al., 2009). Although hosted by the Neoproterozoic Lengjiaxi Group (Wang and Zhou, 2012; Yao et al., 2014; Yang et al., 2015), the Hengdong deposit has an early Cretaceous ore-forming age. This indicates that there might be no genetic relationship between the Hengdong Co mineralization and the metamorphism of the Lengjiaxi Group, because the Neoproterozoic rocks in the JOB have a deformational and metamorphic peak age at ca. 460–420 Ma (Xu et al., 2017).

6.2. Origin of ore-metal Co and fluids

6.2.1. Evidence from pyrite composition

The LA–ICP–MS time-resolved depth profiles of Co, Ni and As are smooth and consistent with that of Fe (Fig. 7a and b), and element mapping by electron microprobe show that Co always couples with a Fe deficiency (Fig. 7c and d), indicating that Co mainly substituted the position of Fe in pyrite. Selenium, Te and As have geochemical affinities or similar charge and ionic radii to S to make them easily enter the lattice of pyrite via replacing S. The concentration of Te in pyrite from

the Hengdong deposit are near the detection limits and is probably caused by the high As and Se contents. Lead and Bi show similar patterns with Fe but they also characterize some anomalies in the time-resolved depth profile (Fig. 7a and b), unraveling that both the Pb and Bi are primarily distributed in pyrite as sulfide inclusions. The ore elements are dominated by Cu, Co, Ni, Ag and Au, with minor Zn and Sb, and higher in the M-stage pyrite, indicating that the initial ore-forming fluids were enriched in these elements. The other transit elements and some immobile elements, like Sc, V, Mn, Ga, Cd and Ba, are more variable in the wall rocks, i.e., both the Lengjiaxi Group and Yanshanian granitoids, suggesting that the ore fluid might interact with wall rocks. Other lithophile elements, like Zr, Rb, U and Ba, might locally exist in the pyrite as silicate inclusions.

The Co and Ni distribution patterns in pyrite may record information on the pyrite-precipitating fluid (Large et al., 2009; Koglin et al., 2010), the chemistry of which are controlled by the primary ore fluid composition and the modifications via wall rock/fluid interaction. In our study, the similar high Co and Ni contents of pyrite from both the wall-rock pyrite (more variable) and M stages of mineralization probably reflect the intensive influence of wall rock/fluid interaction (Table 4), otherwise the wall-rock pyrite will be much lower Co and Ni contents because of the weak ore-forming potential during the wall rock. The Co/Ni ratio in pyrite is also sensitive to environmental change and thus has been used by a school of researchers as an indicator to trace the ore-forming environments (Raymond, 1996; Layton-Matthews et al., 2008). The Co vs. Ni diagram shows that the Hengdong pyrite samples mainly fall into the volcanogenic field and lesser in the hydrothermal field (Fig. 13). This is consistent with that the Co/Ni ratios of the wall-rock pyrite and M-stage pyrite are 1.2–334.3 and 15.0–86.2, respectively, which are quite different from those of the sedimentary pyrites, as defined above. Therefore, the Hengdong deposit genetically is probably closely linked to volcanic rocks due to infiltration of hydrothermal fluids.

6.2.2. Evidence from sulfur and lead isotopic components

The mineral assemblage of quartz + sulfide and no occurrence of sulfate minerals observed in the Hengdong deposit indicate a reducing environment when Co precipitated. In the reducing and medium temperature (< 350 °C) environment, the sulfur isotopic fractionation between sulfides and fluids is usually small (< 2%; Ohmoto and Goldhaber, 1997), which means the measured $\delta^{34}S$ values of sulfides are nearly equal to those of the fluids. Except for two sulfide samples with near-zero $\delta^{34}S$ values (−1.7% and −1.5%) that in many hydrothermal deposits likely indicate a deep-seated sulfur source (Ohmoto, 1972; Chaussidon et al., 1989), which are higher than the majority $\delta^{34}S$ values in the Hengdong deposit (−7.5% to −15.9%). Relative to some of the typical magmatic-hydrothermal deposits, e.g., the Jinchong Co-Cu and Qibaoshan Cu-polymetallic deposits in northeastern Hunan Province, most of $\delta^{34}S$ values of Hengdong deposit are significantly lower (Fig. 14), indicating that the magmatic sulfur is not the main reservoir of the sulfur source. This conclusion is consistent with the large gap between the mineralization age of the Hengdong deposit and the emplacement ages of the Mesozoic plutons in northeastern Hunan Province. Moreover, the observed sulfur isotopic values from the Hengdong deposit are beyond the range of the Banxi Group (Fig. 14), indicating the Banxi Group could not be the sulfur reservoir. The large variation of $\delta^{34}S$ values (Fig. 11) suggests a significant contribution of sulfur from the wall rocks (i.e., the Lengjiaxi Group and the Lianyunshan granitoids). This is supported by the pyrite chemical components, the two near-zero $\delta^{34}S$ values in the Hengdong deposit and the obvious overlapping $\delta^{34}S$ values of sulfides from the Lengjiaxi Group (−13.1 to 24%; Luo et al., 1984; Luo, 1988, 1990; Liu et al., 1994, 1999). Nevertheless, the Lengjiaxi Group could not supply the whole sulfur to the fluids due to the lower sulfur isotopic values in part of pyrites, which is supported by the result of lead isotopic compositions (Fig. 12).

The lead isotope systematics of the Hengdong deposit plot close to the orogenic field but are higher than that of the modern mantle (Fig. 12a). Moreover, the Hengdong ores, Liangyunshan Group, Lianyunshan granitoids as well as the Lengjiaxi Group have more radiogenic Pb than that of mantle and the lower crust (Fig. 12b), revealing the possible source of lead from the upper crust for the Hengdong Co mineralization (e.g., Chen et al., 2008). However, the Pb isotopic ratios of the Lengjiaxi Group are more radiogenic than the Hengdong ores (Fig. 12), indicating that the Co could not be derived from the Lengjiaxi Group. Nevertheless, the lead isotope data of the Hengdong ores show a relative wide scatter but close to or slightly radiogenic than that of the Lianyunshan Group (Fig. 12), probably reflecting a main derivation of the Co from the latter, although a source from the wall rocks could not be excluded. The Pb isotopic features and the near-zero $\delta^{34}S$ values of sulfides from the Hengdong ores might be caused by the interaction between ore fluids and the Liangyunshan granitoids. Combined with the evidence from the trace-element compositions of pyrite and the S and Pb isotopic components, the ore fluids and metal Co most likely originated form the Lianyunshan Group. However, the possible contribution of the Co due to the interaction between the ore fluids and the wall rocks (i.e., the Lengjiaxi Group and Lianyunshan granitoids) cannot be excluded.

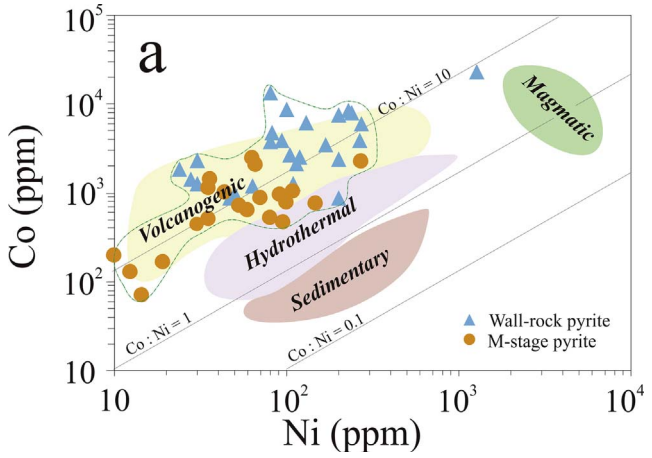

Fig. 13. (a) Co/Ni distribution diagram of pyrite in the Hengdong deposit. Boundaries defining pyrite formed under different geological environments are modified from Bajwah et al. (1987) and Brill (1989).

6.3. Fluid evolution and ore precipitation mechanism

From E- to L-stages, some features of fluid evolution are summarized below. The total homogenization temperatures of fluid inclusions decrease from 250 to 320 °C (peak of 280–300 °C) at the E stage, through ~220–320 °C (peak of 270–300 °C) at the M stage, and to ~150–230 °C at the L stage. The maximum densities of fluid inclusions also have an elevated trend from 0.92 g/cm^3 of the E stage through 0.93 g/cm^3 of the M stage, and to 1.02 g/cm^3 of the L-stage (Fig. 10). However, the salinities and densities of fluid inclusions in quartz from the E- to L stages of mineralization were rarely changed (Table 4 and Fig. 10).

As described earlier, the LV inclusions and V-rich inclusions in the M-stage can occur at a small scale in the same quartz grain, which is important to investigate whether the formation of the different fluid inclusion types are related to fluid immiscibility processes operating on an originally homogeneous single fluid during its entrapment. Alternatively, the heterogeneous entrapment could also have resulted from necking down (Roedder, 1984; Bakker and Jansen, 1994) and the mixing of two or more different original fluids (Anderson et al., 1992). The fluid inclusions in the small area have the constant gas fill and the host quartz (Q3) shows weakly or none deformed, which suggests that the necking-down is unlikely result of heterogeneous entrapment. In

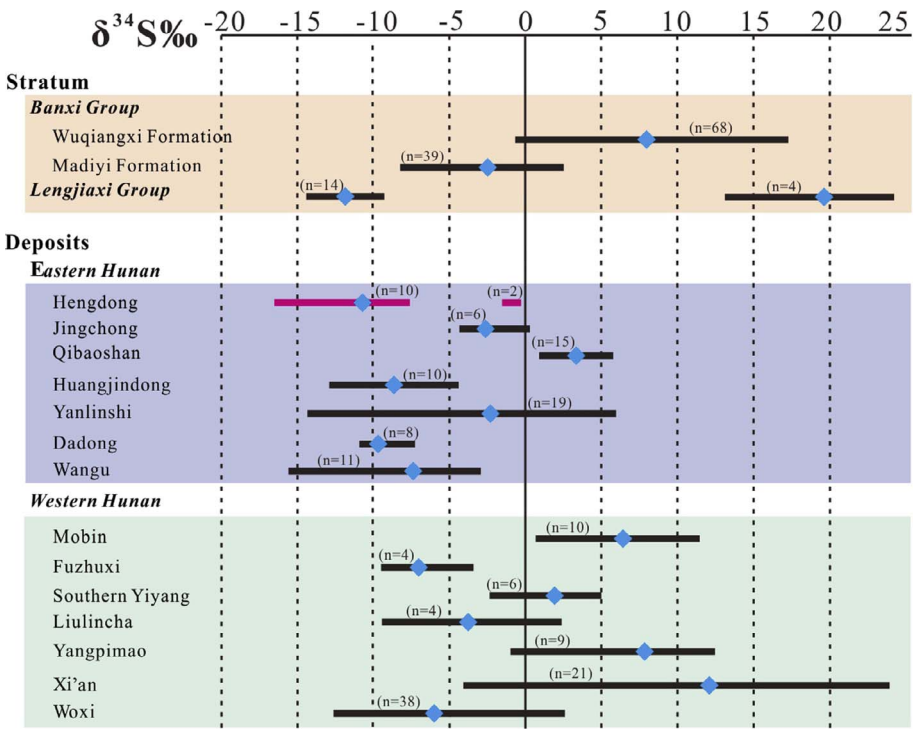

Fig. 14. Distribution of sulfur isotopes for the typical deposits and host rocks from Hunan Province of the JOB. The black bold lines represent the range of S isotope distribution and the blue points represent the average values. Data source: Xu et al. (2017) and references therein. (For interpretation of the references to colour in this figure legend, the reader is referred to the web version of this article.)

addition, the majority of LV and V-rich inclusions in M-stage display the same salinity and density but varying homogenization temperatures. The lack of distinctive fluid inclusion populations that have widely variable in bulk salinity and homogenization temperatures trapped on small area suggests that mixing of fluids from different fluid sources was not a major depositional process (e.g., Fusswinkel et al., 2013).

Based on the criteria outlined by Ramboz et al. (1982), the observations made in this study suggest that fluid immiscibility could be invoked in Hengdong deposit: (1) the LV and V-rich inclusions coexit in a small scale (Figs. f–g), and thus are interpreted to have been trapped contemporaneously; (2) the LV and V-rich inclusions homogenize both in the liquid and vapor phases at about the same temperature range, respectively; (3) the chlorite geothermometric temperature are consistent with the inclusion homogenized temperature, indicating the inclusion was trapped at the bubble-curve (or dew curve) (Tables 2 and 4). The occurrence of the orebodies within fault zones and associated cataclasite and breccias suggests that the P-T-X evolution of the hydrothermal fluid that transported Co in solution was intimately related to physical processes during the reactivation of CPDFZ, which may result of dramatic pressure fluctuations in the fault zone (Baudon and Cartwright, 2008) and then the fluid immiscibility taken place in Hengdong deposit (cf. Hagemann and Lüders, 2003).

Fluid immiscibility, an important mechanism for ore-metal deposition in many hydrothermal deposits. Several researchers (e.g., Reed and Palandri, 2006; Coulibaly et al., 2008) have shown that the immiscibility of hydrothermal fluids can significantly alter the phase equilibrium of the fluids. Phase changes facilitate the decomposition of metal complexes in hydrothermal fluid, causing precipitation of a large amount of metal sulfides. Thus, metallic elements such as Co in the ore fluids for the Hengdong deposit no longer existed as the stable form, and precipitated from the hydrothermal fluid during the M-stage. In addition, fluid immiscibility and hydraulic fracturing commonly caused the uprising ore fluids to decompress and then decrease the temperature (Zhou et al., 2015 and references therein), like the L-stage ore fluids for the Hengdong deposit, which will further advance the precipitation of ore metals.

6.4. The Co mineralization evolution

Approximately coeval with the significant crustal extension and lithospheric thinning in North China during the Early Cretaceous, a widespread extensional event also took place in South China (e.g., Gilder et al., 1991; Li, 2000; Lin et al., 2008). Such an extensional event (s) in South China is supported by the well-developed extensional basins as the Yuanma, Hengyang and Nanxiong basins (Gilder et al., 1991; Shu et al., 2007, 2009; Li et al., 2012a), the exhumation of or metamorphic core complexes (MCCs) as the Dayunshan, Lushan and Hengshan domes (Lin et al., 2000; Shu et al., 2008), and a series of NE- to ENE-trending strike-slip shear faults (Li, 2000). Liu et al. (2016) confirmed that these extension-type structures mainly formed between 130 Ma and 120 Ma. Compared with those in the North China Block, the MCCs are rarely developed in South China, resulting in the extension involved the crust at a relatively shallow level therein (Li et al., 2013). Some of the MCCs such as the Wugongshan, Hongzhen and Xingzi are also well dated at between 130 Ma and 125 Ma (Shen et al., 2008; Liu et al., 2016 and references therein). In addition, abundant A-type granitic and bimodal volcanic rocks as in the Lower Yangtze River belt, JOB, Xiangshan and southeast coastal area (Wong et al., 2009; Jiang et al., 2015b), and the adakite-like rocks formed by melting of a thickened lower crust (Xu et al., 2002; Wang et al., 2006a, 2007b) have the intrusion and/or extrusion ages between 129 Ma and 122 Ma. These ages are consistent with the timing of the Hengdong Co mineralization, indicating an extension environment for the Hengdong deposit.

It has been generally accepted that the Late Mesozoic extensional event(s) in South China was associated with either the slab rollback of the subducted Pacific plate or the slab window opening during the ridge subduction (Gilder et al., 1991; Li and Li, 2007; Li et al., 2010, 2014; Sun et al., 2007, 2010; Tang et al., 2013; Jiang et al., 2015b; Zhao et al., 2016). The subducted direction of the Palaeo-Pacific Plate changed by ~80° from oblique subduction to parallel to the continental margin since ~140 Ma (Koppers et al., 2001; Sun et al., 2007), leading to a gradually closing of the old slab window (Zhao et al., 2016) as well as forming two groups of mineralization during the Cretaceous in South China (Mao et al., 2011, 2013). The older group (145–135 Ma) is

represented by the porphyry-skarn-stratabound Cu-Au-Mo-Fe deposits (Mao et al., 2011), and the younger group (120–80 Ma, with peak at 100–90) includes subvolcanic-related Fe and porphyry Cu-Mo deposits (Mao et al., 2013). Mao et al. (2013) proposed that the time range between 135 Ma and 120 Ma is endowed with weak magmatism and mineralization in most of the SCB. However, similar mineralizing ages to that for the Hengdong deposit have also been reported in the JOB of South China, such as the ^{40}Ar–^{39}Ar ages of ca. 130–127 Ma for the Dayan gold occurrence in northeastern Hunan Province (Xu et al., 2017), the Rb–Sr isochron age of 128 ± 3 Ma and Sm-Nd isochron age of 121 ± 11 Ma for the Xianglushan W deposit in northern Jiangxi Province (Zhang et al., 2008), and the potential mineralization ages of 135–130 Ma for the Dahutang W deposit in Jiangxi Province (Jiang et al., 2015a). In addition, a large number of extensional structures during the early Cretaceous in South China not only controls the distribution of the mineralization in later episode (Mao et al., 2011; Xu et al., 2017), but may have acted as pathways for migration of the ore fluids. Therefore, we suggest that the Early Cretaceous period of 130–120 Ma is also a potential and favorable mineralization episode in South China.

Integrating the characteristics of ore fluids, the origin of Co and fluids and the ore-forming timing, herein, a genetic model is tentatively proposed to explain the formation of the Hengdong deposit in the JOB. With the changing direction of the subducted Palaeo-Pacific Plate, the magmatism and associated mineralization were relatively weak during the period of 130–120 Ma. Nevertheless, a series of NE- to ENE-trending strike-slip shear faults, extensional detachments at the relatively shallow level (e.g., the Hengshan), and basin-and-range style provinces were well developed in the southeast China during this period. Accompanying these extension-related structures, voluminous thermal energy probably was generated to initiate the release of large amounts of Co-bearing fluids from the Neoproterozoic volcanogenic or older metamorphic rocks (i.e. the Lianyunshan Group in the northeastern Province), and then to promote the transportation these ore fluids along the NE–ENE-trending strike-slip faults (i.e., the CPDFZ) in the northeastern Hunan Province of the JOB. Eventually, the fluid immiscibility and gradually decreasing temperatures of the ore fluids could have led to precipitation and enrichment of the metal Co in these extensional structures.

7. Conclusions

1) The Hengdong Co deposit contains three stages of hydrothermal mineralization, i.e., quartz + pyrite + muscovite ± chalcopyrite of the early-stage (E-stage), quartz + polymetallic sulfide + chlorite + of the middle-stage (M-stage), and quartz + chlorite + carbonate of the late-stage (L-stage).
2) The ^{40}Ar–^{39}Ar data reveal that the Hengdong Co mineralization was likely associated with the CPDFZ and formed at the early Cretaceous of ca. 125 Ma age.
3) The ore metal Co was most likely extracted by the ore fluids from the metamafic rocks of the Lianyunshan Group, and contaminated by the fluids reactivated from both the Lengjiaxi Group and Lianyunshan granitiods.
4) The ore fluids were initially mesothermal and then evolved to lower temperatures in the later stages of mineralization.
5) Fluid immiscibility at the Hengdong deposit is considered to be the result of significant cyclic pressure reduction during fault zone movement (probably seismic pumping), thereby reducing the degree of cobalt under-saturation, and causes cobalt to precipitate.
6) The early Cretaceous period of 130–120 Ma was also a potential mineralization age in South China. The development of extension-type structures at ca. 130–120 Ma is favorable of the immigration of the ore fluids and the precipitation and enrichment of the ore metal along the NE- to ENE-trending strike-slip faults.

Acknowledgments

This research was financially co-supported by the Deep Resource Exploration and Mining (DREAM) project of MOST China (2016YFC0600401) and the Chinese Ministry of Land and Resources (1212011220710). The authors sincerely thank Guojun Tong for the field investigation. We are also grateful of Lingjun Zeng and Changming Xing due to their laboratory help. A particular thank is given to two reviewers for their thorough and constructive reviews, and Editor-in-Chief Franco Pirajno for his editorial handling of the paper. The first author thanks the support of UCAS Joint PhD Training Program (UCAS [2015]37) for providing the living expenses in Canada and the helps from the group of co-supervisor Dr. Iain M. Samson.

Appendix A. Supplementary data

Supplementary data associated with this article can be found, in the online version, at http://dx.doi.org/10.1016/j.oregeorev.2017.11.008.

References

Al-Khirbash, S., 2015. Genesis and mineralogical classification of Ni-laterites, Oman Mountains. Ore Geol. Rev. 65, 199–212.
Anderson, M.R., Rankin, A.H., Spiro, B., 1992. Fluid mixing in the generation of isothermal gold mineralization in the Transvaal Sequence, Transvaal, South Africa. Eur. J. Mineral. 4, 933–948.
Bajwah, Z., Seccombe, P., Offler, R., 1987. Trace element distribution Co: Ni ratios and genesis of the Big Cadia iron-copper deposit, New South Wales, Australia. Miner. Deposita 22, 292–300.
Bakker, R.J., Jansen, J.B.H., 1994. A mechanism for preferential H2O leakage from fluid inclusions in quartz, based on TEM observations. Contrib. Mineral. Petrol. 116, 7–20.
Battaglia, S., 1999. Applying X-ray geothermometer diffraction to a chlorite. Clays Clay Miner. 47, 54–63.
Baudon, C., Cartwright, J., 2008. The kinematics of reactivation of normal faults using high resolution throw mapping. J. Struct. Geol. 30, 1072–1084.
Bodnar, R.J., 1994. Synthetic fluid inclusions: XII. The system H2O NaCl. Experimental determination of the halite liquidus and isochores for a 40 wt% NaCl solution. Geochim. Cosmochim. Acta 58, 1053–1063.
Brill, B.A., 1989. Trace-element contents and partitioning of elements in ore minerals from the CSA Cu–Pb–Zn deposit, Australia. Can. Mineral. 27, 263–274.
Cathelineau, M., Nieva, D., 1985. A chlorite solid solution geothermometer the Los Azufres (Mexico) geothermal system. Contrib. Miner. Petrol. 91, 235–244.
Chaussidon, M., Albarède, F., Sheppard, S.M., 1989. Sulphur isotope variations in the mantle from ion microprobe analyses of micro-sulphide inclusions. Earth Planet. Sci. Lett. 92, 144–156.
Chen, J.F., Jahn, B.M., 1998. Crustal evolution of southeastern China: evidence from Sr, Nd, Pb isotopic compositions of granitoids and sedimentary rocks. Tectonophysics 284, 101–133.
Chen, Y.J., Pirajno, F., Qi, J.P., 2008. The Shanggong gold deposit, Eastern Qinling Orogen, China: isotope geochemistry and implications for ore genesis. J. Asian Earth Sci. 33, 252–266.
Coulibaly, Y., Boiron, M.C., Cathelineau, M., Kouamelan, A.N., 2008. Fluid immiscibility and gold deposition in the Birimian quartz veins of the Angovia deposit (Yaouré, Ivory Coast). J. Afr. Earth Sc. 50, 234–254.
Deer, W.A., Howie, R.A., Zussman, J., 1992. An Introduction to Rock-Forming Minerals. Longman, p. 696.
Deng, T., Xu, D., Chi, G., Wang, Z., Jiao, Q., Ning, J., Dong, G., Zou, F., 2017. Geology, geochronology, geochemistry and ore genesis of the Wangu gold deposit in northeastern Hunan Province, Jiangnan Orogen, South China. Ore Geol. Rev. 88, 619–637.
Dzemua, G.L., Gleeson, S.A., 2012. Petrography, mineralogy, and geochemistry of the Nkamouna serpentinite: implications for the formation of the cobalt-manganese laterite deposit, southeast Cameroon. Econ. Geol. 107, 25–41.
Feng, C.Y., Zhang, D.Q., 2002. Cobalt mineral resources in the world and advance of the research on cobalt deposits. Geol. Rev. 48, 627–633 (in Chinese with English abstract).
Fu, G.-G., 2001, Geological characteristics of cobalt polymetallic deposit and its prospecting index at Pule, Liuyang. Hunan Geology.
Fu, Z.R., Li, Z.J., Zhen, D.Y., 1999. Structural pattern and tectonic evolution of NNE-trending strike-slip or ogenic belt in the border region of Hunan and Jiangxi Province. Earth Sci. Front. 6 (4), 263–272 (in Chinese with English abstract).
Fusswinkel, T., Wagner, T., Wälle, M., Wenzel, T., Heinrich, C.A., Markl, G., 2013. Fluid mixing forms basement-hosted Pb-Zn deposits: insight from metal and halogen geochemistry of individual fluid inclusions. Geology 41, 679–682.
Gao, L.Z., Yang, M.G., Ding, X.Z., Liu, Y.X., Liu, X., Ling, L.H., Zhang, C.H., 2008. SHRIMP U-Pb zircon dating of tuff in the Shuangqiaoshan and Heshangzhen groups in South China-constraints on the evolution of the Jiangnan Neoproterozoic orogenic belt. Geol. Bull. China 27, 1744–1751.
Gao, L.Z., Chen, J., Ding, X.Z., Liu, Y.R., Zhang, C.H., Zhang, H., Liu, Y.X., Pang, W.H., Zhang, Y.H., 2011. Zircon SHRIMP U-Pb dating of the tuff bed of Lengjiaxi and Banxi

groups, northeastern Hunan: constraints on the Wuling Movement. Geol. Bull. China 30, 1001–1008.
Gilder, S.A., Keller, G.R., Luo, M., Goodell, P.C., 1991. Eastern Asia and the Western Pacific timing and spatial distribution of rifting in China. Tectonophysics 197, 225–243.
Goldstein, R.H. and Reynolds, T.J., 1994, Systematics of Fluid Inclusions in Diagenetic Minerals.
Guan, Y., Yuan, C., Sun, M., Wilde, S., Long, X., Huang, X., Wang, Q., 2014. I-type granitoids in the eastern Yangtze Block: implications for the Early Paleozoic intracontinental orogeny in South China. Lithos 206–207, 34–51.
Hagemann, S.G., Lüders, V., 2003. P-T-X conditions of hydrothermal fluids and precipitation mechanism of stibnite-gold mineralization at the Wiluna lode-gold deposits, Western Australia: conventional and infrared microthermometric constraints. Miner. Deposita 38, 936–952.
He, Z.L., Xu, D.R., Chen, G.H., Xia, B., Li, P.C., Fu, G.G., 2004. Gold poly-metallicore-forming geochemistry of the Yanshanian intra-continental collision orogen, northeastern Hunan Province. Miner. Deposits 23 (1), 39–51.
HNBGMR (Hunan Bureau of Geology and Mineral Resources), 1988. Regional Geology of Hunan Province. Geological Publishing House, Beijing, pp. 6–30 (in Chinese).
Hu, M.-Y., He, H.-L., Zhan, X.-C., Fan, X.-T., Wang, G., Jia, Z.-R., 2008. Matrix normalization for in-situ multi-element quantitative analysis of zircon in laser ablation–inductively coupled plasma mass spectrometry. Chin. J. Anal. Chem. 36, 947–953.
Jia, B.H., Peng, H.Q., 2005. Precambrian geology and metallogenesis in northeastern Hunan Province. Geology Publishing House, Beijing, pp. 1–138 (in Chinese).
Jia, D., Hu, R., Zhao, J., Xie, G., 2003. Lithogeochemical characteristics of the Mesozoic granitic intrusion from the Wangxiang area in Northeastern Hunan Province and its tectonic setting. Acta Geol. Sinica 77, 98–103 (in Chinese with English abstract).
Jiang, S.Y., Peng, N.J., Huang, L.C., Xu, Y.M., Zhan, G.L., Dan, X.H., 2015a. Geological characteristic and ore genesis of the giant tungsten deposits from the Dahutang ore-concentrated district in northern Jiangxi Province. Acta Petrol. Sin. 31, 639–655.
Jiang, Y.-H., Wang, G.-C., Liu, Z., Ni, C.-Y., Qing, L., Zhang, Q., 2015b. Repeated slab advance–retreat of the Palaeo-Pacific plate underneath SE China. Int. Geol. Rev. 57, 472–491.
Jin, W., Zhang, L., 2000, Study on rock- and ore-controlling structures in northeast Hunan Province, South China. Geology & Mineral Resources of South China (in Chinese).
Klein, E.L., Harris, C., Giret, A., Moura, C.A.V., 2007. The Cipoeiro gold deposit, Gurupi Belt, Brazil: Geology, chlorite geochemistry, and stable isotope study. J. S. Am. Earth Sci. 23, 242–255.
Koglin, N., Frimmel, H.E., Minter, W.E.L., Braetz, H., 2010. Trace-element characteristics of different pyrite types in Mesoarchaean to Palaeoproterozoic placer deposits. Miner. Deposita 45, 259–280.
Koppers, A.A., 2002. ArArCALC—software for 40 Ar/39 Ar age calculations. Comput. Geosci. 28, 605–619.
Koppers, A.A.P., Morgan, J.P., Morgan, J.W., Staudigel, H., 2001. Testing the fixed hotspot hypothesis using 40Ar/39Ar age progressions along seamount trails. Earth Planet Sci. Lett. 185, 237–252.
Large, R.R., Danyushevsky, L., Hollit, C., Maslennikov, V., Meffre, S., Gilbert, S., Bull, S., Scott, R., Emsbo, P., Thomas, H., Singh, B., Foster, J., 2009. Gold and trace element zonation in pyrite using a laser imaging technique: implications for the timing of gold in orogenic and carlin-style sediment-hosted deposits. Econ. Geol. 104, 635–668.
Layton-Matthews, D., Peter, J.M., Scott, S.D., Leybourne, M.I., 2008. Distribution, mineralogy, and geochemistry of selenium in felsic volcanic-hosted massive sulfide deposits of the Finlayson Lake district, Yukon Territory, Canada. Econ. Geol. 103, 61–88.
Li, X.-H., 2000. Cretaceous magmatism and lithospheric extension in Southeast China. J. Asian Earth Sci. 18, 293–305.
Li, Z.X., Li, X.H., 2007. Formation of the 1300-km-wide intracontinental orogen and postorogenic magmatic province in Mesozoic South China: a flat-slab subduction model. Geology 35, 179–182.
Li, X.H., Li, W.X., Li, Z.X., Lo, C.H., Wang, J., Ye, M.F., Yang, Y.H., 2009. Amalgamation between the Yangtze and Cathaysia Blocks in South China: constraints from SHRIMP U-Pb zircon ages, geochemistry and Nd-Hf isotopes of the Shuangxiwu volcanic rocks. Precambr. Res. 174, 117–128.
Li, X.-H., Li, W.-X., Wang, X.-C., Li, Q.-L., Liu, Y., Tang, G.-Q., Gao, Y.-Y., Wu, F.-Y., 2010. SIMS U-Pb zircon geochronology of porphyry Cu–Au–(Mo) deposits in the Yangtze River Metallogenic Belt, eastern China: magmatic response to early Cretaceous lithospheric extension. Lithos 119, 427–438.
Li, J., Zhang, Y., Dong, S., Li, H., 2012a. Late Mesozoic-Early Cenozoic deformation history of the Yuanma Basin, central South China. Tectonophysics 163–183.
Li, J.W., Bi, S.J., Selby, D., Chen, L., Vasconcelos, P., Thiede, D., Zhou, M.F., Zhao, X.F., Li, Z.K., Qiu, H.N., 2012b. Giant Mesozoic gold provinces related to the destruction of the North China craton. Earth Planet Sci. Lett. 349, 26–37.
Li, J., Zhang, Y., Dong, S., Su, J., Li, Y., Cui, J., Shi, W., 2013. The Hengshan low-angle normal fault zone: structural and geochronological constraints on the Late Mesozoic crustal extension in South China. Tectonophysics 606, 97–115.
Li, J., Zhang, Y., Dong, S., Johnston, S.T., 2014. Cretaceous tectonic evolution of South China: a preliminary synthesis. Earth Sci. Rev. 134, 98–136.
Li, J.-H., Zhang, Y.-Q., Dong, S.-W., Ma, Z.-L., Li, Y., 2015. LA-MC-ICPMS Zircon U-Pb Geochronology of the Hongxiaqiao and Banshanpu Granitoids in Eastern Hunan Province and its geological implications. Acta Geosci. Sin. 36, 187–196 (in Chinese with English abstract).
Lin, W., Sun, Y., Moni, P., Faure, M., Zhang, L., 2000. Tectonics of SE China: new insights from the Lushan massif (Jiangxi Province). Tectonics 852–871.
Lin, W., Wang, Q., Chen, K., 2008, Phanerozoic tectonics of south China block: New insights from the polyphase deformation in the Yunkai massif. Tectonics, 27.
Liu, D., Wu, Y., Liu, S., 1994. Geochemistry of Wangu gold deposit. Hunan Geol. 16, 83–90 (in Chinese with English abstract).
Liu, Y., Peng, L., Wu, S., 1999. Genetic features for mine vein-type gold deposits in northeastern Hunan. J. Cent. South Univ. Technol. (Nat. Sci.) 30, 4–7.
Liu, S., Zhu, G., Wu, Q., Chen, Y., Zhang, S., Wang, W., 2016. Reappraisal of Protolith ages and formation mechanism for the metamorphic core complex in Hongzhen, Huaining County, Anhui Province. Geol. Rev. 62, 585–603.
Luo, X.L., 1988. The genesis and model of Huangjindong gold deposit in Hunan Province. J. Guilin Coll. Geol. 8 (8), 225–239 (in Chinese with English abstract).
Luo, X.L., 1990. The source of ore-forming substances of Precambrian gold deposits in Hunan Province. J. Guilin Coll. Geol. 10 (01), 13–26 (in Chinese with English abstract).
Luo, X.L., Yi, S.J., Liang, J.C., 1984. The genesis of Woxi Sb-W gold deposits in western Hunan province, South China. J. Guilin Coll. Geol. 1, 21–37 (in Chinese with English abstract).
Mao, J.W., Pirajno, F., Cook, N., 2011. Mesozoic metallogeny in East China and corresponding geodynamic settings – an introduction to the special issue. Ore Geol. Rev. 43, 1–7.
Mao, J.W., Cheng, Y.B., Chen, M.H., Pirajno, F., 2013. Major types and time-space distribution of Mesozoic ore deposits in South China and their geodynamic settings. Miner. Deposita 48, 267–294.
Marques, A.F.A., Barriga, F.J.A.S., Scott, S.D., 2007. Sulfide mineralization in an ultramafic-rock hosted seafloor hydrothermal system: from serpentinization to the formation of Cu–Zn–(Co)-rich massive sulfides. Mar. Geol. 245 (1), 20–39.
McDougall, I., Harrison, T.M., 1999, Geochronology and Thermochronology by the 40Ar/39Ar Method. Oxford University Press on Demand.
Naldrett, A., 1999. World-class Ni–Cu–PGE deposits: key factors in their genesis. Miner. Deposita 34, 227–240.
Naldrett, A.J., Singh, J., Krstic, S., Li, C., 2000. The mineralogy of the Voisey's Bay Ni–Cu–Co deposit, northern Labrador, Canada: influence of oxidation state on textures and mineral compositions. Econ. Geol. 95 (4), 889–900.
Ning, J.T., 2002. The native cobalt mineralization and geological condition analysis in Northeast Hunan Province, South China. Hunan Geol. 03, 192–195 (In Chinese).
Ohmoto, H., 1972. Systematics of sulfur and carbon isotopes in hydrothermal ore deposits. Econ. Geol. 67, 551–578.
Ohmoto, H., Goldhaber, M.B., 1997. Sulfur and carbon isotopes. In: Barnes, H.L. (Ed.), Geochemistry of Hydrothermal Ore Deposits. Wiley Interscience, New York, pp. 435–486.
Peng, H.Q., Jia, B.H., Tang, X.S., 2004. Uplift process of Mufushan and thermochronology of Wangxiang granites in northeastern Hunan Province. Geol. Sci. Technol. Inf. 23, 11–15.
Potter, R.W., Clynne, M.A., Brown, D.L., 1978. Freezing point depression of aqueous sodium chloride solutions. Econ. Geol. 73, 284–285.
Qiu, H.N., Jiang, Y.D., 2007. Sphalerite Ar-40/Ar-39 progressive crushing and stepwise heating techniques. Earth Planet Sci. Lett. 256, 224–232.
Qiu, H.N., Wijbrans, J.R., Brouwer, F.M., Yun, J.B., Zhao, L.H., Xu, Y.G., 2010. Amphibolite facies retrograde metamorphism of the Zhujiachong eclogite, SE Dabieshan: 40Ar/39Ar age constraints from argon extraction using UV-laser microprobe, in vacuo crushing and stepwise heating. J. Metamorph. Geol. 28, 477–487.
Ramboz, C., Pichavant, M., Weisbrod, A., 1982. Fluid immiscibility in natural processes: use and misuse of fluid inclusion data: II. Interpretation of fluid inclusion data in terms of immiscibility. Chem. Geol. 37, 29–48.
Raymond, O.L., 1996. Pyrite composition and ore genesis in the Prince Lyell copper deposit, Mt Lyell mineral field, western Tasmania, Australia. Ore Geol. Rev. 10, 231–250.
Reed, M.H., Palandri, J., 2006. Sulfide mineral precipitation from hydrothermal fluids. Rev. Mineral. Geochem. 61, 609–631.
Renne, P.R., Cassata, W.S., Morgan, L.E., 2009. The isotopic composition of atmospheric argon and Ar-40/Ar-39 geochronology: time for a change? Quat. Geochronol. 4, 288–298.
Roedder, J., 1984. Fluid inclusions. Rev. Mineral. 1–644.
Shen, X.M., Zhang, H.X., Zhang, B.Y., 2008. A preliminary study of relationship between metamorphic core complexes and lithospheric thinning over the Mesozoic in South China. Geotectonica Metall. 116, 11–19.
Shi, H.C., Shi, X.B., Yang, X.Q., Jiang, H.Y., 2013. The Exhumation process of Mufushan Granite in Jiangnan Uplift Since Cenozoic: evidence from low-temperature thermochronology. Chin. J. Geophys. 56, 273–286.
Shu, L.S., Zhou, X.M., Deng, P., Zhu, W.B., 2007. Mesozoic-Cenozoic Basin features and evolution of Southeast China. Acta Geol. Sin.-Engl 81, 573–586.
Shu, L., Faure, M., Wang, B., Zhou, X., Song, B., 2008. Late Palaeozoic-Early Mesozoic geological features of South China: response to the Indosinian collision events in Southeast Asia. C.R. Geosci. 340, 151–165.
Shu, L.S., Zhou, X.M., Deng, P., Wang, B., Jiang, S.Y., Yu, J.H., Zhao, X.X., 2009. Mesozoic tectonic evolution of the Southeast China Block: new insights from basin analysis. J. Asian Earth Sci. 34, 376–391.
Steiger, R.H., Jager, E., 1977. Subcommission on geochronology – convention on use of decay constants in geochronology and cosmochronology. Earth Planet Sci. Lett. 36, 359–362.
Sun, W., Ding, X., Hu, Y.-H., Li, X.-H., 2007. The golden transformation of the Cretaceous plate subduction in the west Pacific. Earth Planet Sci. Lett. 262, 533–542.
Sun, W., Ling, M., Yang, X., Fan, W., Ding, X., Liang, H., 2010. Ridge subduction and porphyry copper-gold mineralization: an overview. Sci. China Earth Sci. 53, 475–484.
Tang, Y.-J., Zhang, H.-F., Ying, J.-F., Su, B.-X., Li, X.-H., Santosh, M., 2013. Rapid eruption of the Ningwu volcanics in eastern China: response to Cretaceous subduction of the Pacific plate. Geochem. Geophys. Geosyst. 14, 1703–1721.
Wang, W., Zhou, M.F., 2012. Sedimentary records of the Yangtze Block (South China) and their correlation with equivalent Neoproterozoic sequences on adjacent continents.

Sed. Geol. 265, 126–142.
Wang, Y.J., Fan, W.M., Guo, F., Peng, T.P., Li, C.W., 2003. Geochemistry of Mesozoic mafic rocks around the Chenzhou-Linwu fault in South China: implication for the lithospheric boundary between the Yangtze and the Cathaysia Blocks. Int. Geol. Rev. 45, 263–286.
Wang, Q., Wyman, D.A., Xu, J.-F., Zhao, Z.-H., Jian, P., Xiong, X.-L., Bao, Z.-W., Li, C.-F., Bai, Z.-H., 2006a. Petrogenesis of Cretaceous adakitic and shoshonitic igneous rocks in the Luzong area, Anhui Province (eastern China): implications for geodynamics and Cu–Au mineralization. Lithos 89, 424–446.
Wang, X.L., Zhou, J.C., Qiu, J.S., Zhang, W.L., Liu, X.M., Zhang, G.L., 2006b. LA-ICP-MS U-Pb zircon geochronology of the Neoproterozoic igneous rocks from Northern Guangxi, South China: implications for tectonic evolution. Precambr. Res. 145 (1), 111–130.
Wang, X.L., Zhou, J.C., Griffin, W.L., Wang, R.C., Qiu, J.S., O'Reilly, S.Y., Xu, X., Liu, X.M., Zhang, G.L., 2007a. Detrital zircon geochronology of Precambrian basement sequences in the Jiangnan orogen: dating the assembly of the Yangtze and Cathaysia Blocks. Precambr. Res. 159, 117–131.
Wang, Q., Wyman, Derek A., Xu, J.F., Zhao, Z.H., Jian, P., Zi, F., 2007b. Partial melting of thickened or delaminated lower crust in the Middle of Eastern China: implications for Cu-Au mineralization. J. Geol. 115, 149–161.
Wang, X., Zhou, J., Qiu, J., Shi, S., Jiang, Y., 2008. Geochronology and geochemistry of Neoproterozoic mafic rocks from western Hunan, South China: implications for petrogenesis and post-orogenic extension. Geol. Mag. 145, 215–233.
Wang, L.J., Yu, J.H., Griffin, W.L., O'Reilly, S.Y., 2011a. Early crustal evolution in the western Yangtze Block: evidence from U-Pb and Lu–Hf isotopes on detrital zircons from sedimentary rocks. Precambr. Res. 222, 368–385.
Wang, L.-X., Ma, C.-Q., Zhang, C., Zhang, J.-Y., Marks, M.A.W., 2014. Genesis of leucogranite by prolonged fractional crystallization: a case study of the Mufushan complex, South China. Lithos 206–207, 147–163.
Wang, Z., Xu, D., Chi, G., Shao, Y., Lai, J., Deng, T., Guo, F., Wang, Z., Dong, G., Ning, J., Zou, S., 2017. Mineralogical and isotopic constraints on the genesis of the Jingchong Co–Cu polymetallic ore deposit in northeastern Hunan Province, South China. Ore Geol. Rev. 88, 638–654.
Wiewióra, A., Weiss, Z., 1990. Crystallochemical classifications of phyllosilicates based on the unified system of projection of chemical-composition: II. The chlorite group. Clay Miner. 25, 83–92.
Wong, J., Sun, M., Xing, G., Li, X.-H., Zhao, G., Wong, K., Yuan, C., Xia, X., Li, L., Wu, F., 2009. Geochemical and zircon U-Pb and Hf isotopic study of the Baijuhuajian metaluminous A-type granite: extension at 125–100 Ma and its tectonic significance for South China. Lithos 112, 289–305.
Xu, J.-F., Shinjo, R., Defant, M.J., Wang, Q., Rapp, R.P., 2002. Origin of Mesozoic adakitic intrusive rocks in the Ningzhen area of east China: partial melting of delaminated lower continental crust? Geology 30, 1111–1114.
Xu, D.R., Gu, X.X., Li, P.C., Chen, G.H., 2007. Mesoproterozoic-Neoproterozoic transition: geochemistry, provenance and tectonic setting of clastic sedimentary rocks in southeastern Margin of the Yangtze Block, South China. J. Asian Earth Sci. 29, 637–650.
Xu, D.R., Wang, L., Li, P.C., Chen, G.H., He, Z.L., Fu, G.G., Wu, J., 2009. Petrogenesis of the Lianyunshan granites in northeastern Hunan Province, South China, and its geodynamic implications. Acta Petrol. Sin. 25, 1056–1078 (in Chinese with English abstract).
Xu, D., Deng, T., Chi, G., Wang, Z., Zou, F., Zhang, J., Zou, S., 2017. Gold mineralization in the Jiangnan Orogenic Belt of South China: geological, geochemical and geochronological characteristics, ore deposit-type and geodynamic setting. Ore Geol. Rev. 88, 565–618.
Yang, C., Li, X.H., Wang, X.C., Lan, Z.W., 2015. Mid-Neoproterozoic angular unconformity in the Yangtze Block revisited: insights from detrital zircon U-Pb age and Hf-O isotopes. Precambrian Res. 266, 165–178.
Yao, J.L., Shu, L.S., Santosh, M., Zhao, G.C., 2014. Neoproterozoic arc-related mafic-ultramafic rocks and syn-collision granite from the western segment of the Jiangnan Orogen, South China: constraints on the Neoproterozoic assembly of the Yangtze and Cathaysia Blocks. Precambrian Res. 243, 39–62.
Yavuz, F., Kumral, M., Karakaya, N., Karakaya, M.Ç., Yıldırım, D.K., 2015. A Windows program for chlorite calculation and classification. Comput. Geosci. 81, 101–113.
Yi, Z.S., Luo, X.Y., Zhou, D.H., Xiao, C.Y., 2010, Geological Characteristics and Genesis of Jinchong Co-Cu Polymetal Deposit,Liuyan,Hunan Province. Geology & Mineral Resources of South China (in Chinese).
Zane, A., Weiss, Z., 1998. A procedure for classifying rock-forming chlorites based on microprobe data. Rendiconti Lincei 9, 51–56.
Zang, W., Fyfe, W.S., 1995. Chloritization of the hydrothermally altered bedrock at the Igarape-Bahia Gold Deposit, Carajas, Brazil. Miner. Deposita 30, 30–38.
Zartman, R.E., Doe, B.R., 1981. Plumbotectonics – the Model. Tectonophysics 75, 135–162.
Zartman, R.E., Haines, S.M., 1988. The Plumbotectonic model for Pb isotopic systematics among major terrestrial reservoirs – a case for bi-directional transport. Geochim. Cosmochim. Acta 52, 1327–1339.
Zhang, W.S., 1991. The fracture structure and geochemical characteristics of dynamic metamorphic belt in Changsha-Pinjiang fault in Northeast Hunan. Geotectonica Metall. 02, 100–109 (in Chinese with English abstract).
Zhang, S.-B., Zheng, Y.-F., 2013. Formation and evolution of Precambrian continental lithosphere in South China. Gondwana Res. 23, 1241–1260.
Zhang, J., Mei, Y., Wang, D., Li, H., 2008. Isochronology study on the Xianglushan scheelite deposit in North Jiangxi Province and its geological significance. Acta Geol. Sin. 82, 927–931.
Zhang, Y., Wang, Y., Fan, W., Zhang, A., Ma, L., 2012. Geochronological and geochemical constraints on the metasomatised source for the Neoproterozoic (~825 Ma) high-mg volcanic rocks from the Cangshuipu area (Hunan Province) along the Jiangnan domain and their tectonic implications. Precambrian Res. 220, 5–12.
Zhao, G., 2015. Jiangnan Orogen in South China: developing from divergent double subduction. Gondwana Res. 27, 1173–1180.
Zhao, G., Cawood, P.A., 2012. Precambrian geology of China. Precambrian Res. 222, 13–54.
Zhao, L., Guo, F., Fan, W., Zhang, Q., Wu, Y., Li, J., Yan, W., 2016. Early Cretaceous potassic volcanic rocks in the Jiangnan Orogenic Belt, East China: crustal melting in response to subduction of the Pacific-Izanagi ridge? Chem. Geol. 437, 30–43.
Zhou, J.C., Wang, X.L., Qiu, J.S., 2009. Geochronology of Neoproterozoic mafic rocks and sandstones from northeastern Guizhou, South China: Coeval arc magmatism and sedimentation. Precambrian Res. 170, 27–42.
Zhou, Z.J., Chen, Y.J., Jiang, S.Y., Hu, C.J., Qin, Y., Zhao, H.X., 2015. Isotope and fluid inclusion geochemistry and genesis of the Qiangma gold deposit, Xiaoqinling gold field, Qinling Orogen, China. Ore Geol. Rev. 66, 47–64.